Max Planck Institute for Solid State Research Stuttgart

Characterization of Carbon Nanotube Gas Diffusion Electrodes in Low Temperature H_2/O_2 Fuel Cells

Michael Lebert

Autonomous University of Madrid, 2009

Dpt. of Applied Physics and Chemistry, Autonomous University of Madrid (UAM)
PhD programme "Applied Physics and Chemistry"

Professors: Prof. Dr. José Luis Garcia Fierro
Prof. Dr. Norbert Nicoloso

Date: 12 January 2009

List of Publications

This work can be partly reviewed in:

M. Lebert, M. Kaempgen, M. Soehn, T. Wirth, S. Roth, N. Nicoloso, Fuel Cell Electrodes using Carbon Nanostructures, *Catalysis Today,* in Press, online 23 December (2008)

M. Kaempgen, M. Lebert, M. Haluska, V. Siegle, N. Nicoloso, S. Roth, Sonochemical Optimization of the Conductivity of Single-Wall Carbon Nanotube Networks, *Advanced Materials*, 20, 616 (2008)

M. Soehn, M. Lebert, T. Wirth, S. Hofmann, N. Nicoloso, Design of Gas Diffusion Electrodes using Nanocarbon, *Journal of Power Sources, 176, 494 (2008)*

M. Kaempgen, M. Lebert, N. Nicoloso, S. Roth, Multifunctional carbon nanotube networks for fuel cells, *Applied Physics Letters*, 92, 094103 (2008)

M. Kaempgen, M. Lebert, S. Roth, M. Soehn, N. Nicoloso, Fuel cells based on multifunctional carbon nanotube networks, *Journal of Power of Sources*, 180, 755 (2008)

M. Haluška, D. Obergfell, J.C. Meyer, G. Scalia, G. Ulbricht, B. Krauss, D.H. Chae, T. Lohmann, M. Lebert, M. Kaempgen, J. Smet, M. Hulman, S. Roth, K. von Klitzing, Investigation of the shift of Raman modes of graphene flakes, *physica status solidi (b)*, 244, 11, 4143 (2007)

S. Roth, M. Kaempgen, M. Lebert, N. Nicoloso, German patent application, *10 2007 012 235.9-45* (2007)

Acknowledgements

These people are the fundament of this work, they supported and teached me a lot:

I am indebted to my supervisors Prof. Dr. José Luis Garcia Fierro, Autonomous University of Madrid, ICP/CSIC and Prof. Dr. Norbert ('Nico') Nicoloso, Technical University of Darmstadt for giving me a high degree of freedom and scientic support.

I am very thankful to Dr. Siegmar Roth, Max Planck Institute for Solid State Research, department of Prof. Dr. Klaus v. Klitzing, for giving me the excellent opportunity to work within his group 'Synthetic Nanostructures'.

I am grateful to Prof. Dr. Ernesto Diez and Prof. Dr. Enrique Fatás Lahoz for opening the door to the scientific campus of the Autónoma.

I would like to thank:
Dr. Martti Kaempgen for the intensive collaboration, important advice and critical motivitation. Dr. Miroslav ('Miro') Haluska for intensive Raman measurements and discussions and for providing isolated SWNTs. Matthias Söhn for adhoc IT-supports and engineering advices. Serhat Sahakalkan for AFM guidance and discussions, Dirk Obergfell for providing AFM data of isolated SWNTs, Alberto Ansaldo for AFM section analysis. Prof. Dr. Viera Skakalova for discussions about functionalized SWNTs, Dr. Ursula Dettlaff for the assistance of buckypaper preparation.

Siegfried Graf for fuel cell array construction and Stefan Anderle for fuel cell testing software (both DLR, Stuttgart), Miguel Peña for early XPS measurements (ICP/CSIC, Madrid), Georg Düsberg for nicely grown large-scale MWNT samples (Infineon, München).

Manfred Schmidt for adhoc technical solutions and Helmut Kammerlander for immediate support related to all kinds of glass (all MPI).

Achim Klein-Hoffmann,Norbert Pfänder and Dr. Dangsheng Su for providing TEM and SEM pictures (FHI), Gerhard Ulbricht (MPI) for parylene coating, Georg Düsberg for the aligned growth of MWNT on SiO_2

The *4C11 colleagues* Prof. Dr. Viera Skakalova, Dr. Ursula Dettlaff, Dr. Yun Sung Woo, Prof. Nuria Ferrer-Anglada, Alberto Ansaldo, Björn Hornbostel, Chen Wei Liang, Chin-Ching Lin, Dirk Obergfell, Ekkehard Palmer, Jannik Meyer, Jiri Cech, Kun-Ping Huang, Serhat Sahakalkan, Viktor Siegle.

And finally, of course, I thank my wife Áurea for her long patience and tolerance, my parents and sister for their permanent encouragement.

Involved institutes

- *Max Planck Institute for Solid State Research* (MPI), Synthetic Nanostructures, Stuttgart
- *University of Madrid* (UAM), Dpt. of Applied Chemistry and Physics
- *Institute of Catalysis* (ICP/CSIC), Catalysts Structure and Reactivity, Madrid
- *Technical University of Darmstadt* (TUD), Darmstadt
- *Deutsche Luft- und Raumfahrt* (DLR), Stuttgart
- *Infineon*, München
- *Fritz-Haber Institute (FHI)*, Dpt. of Inorganic Chemistry, Berlin

Financial support

The financial support by the EU project CANAPE (Contract No. 500096) is gratefully acknowledged.

Contents

List of Publications

Acknowledgements

1 Introduction

Starting point

Carbon nanotubes (CNTs) [1,2,3] and *fuel cells* [4,5,6] are considered as possible key materials and applications of the future. Recently discovered CNTs offer interesting properties for *H_2/O_2 fuel cell electrodes* such as high specific surface, high aspect ratio, high electronic conductivity and high chemical stability. Such properties make *single-walled carbon nanotubes* (SWNT) networks an interesting alternative to regular electrode materials. Fuel cells with the direct conversion of chemical to electrical energy have significant efficiency advantages compared to combustion engines, especially in temperature ranges where the Carnot efficiency is rather low ($T << 1000$ °C).

In low temperature fuel cells ($T < 100$ °C), *amorphous carbon* (a-C) is commonly used as catalyst support (carbon black) and gas diffusion layer (carbon fibers). In heterogeneous catalysis a-C acts as easily processable, inexpensive and chemically stable support, in electrocatalysis additionally as electrode/ current collector. In H_2-based fuel cells the electrodes further have to allow fast diffusion of the gases hydrogen and oxygen (or air). The main properties of a-C *gas diffusion electrodes* (GDEs) like electrochemical stability, metallic conductivity, density, morphology (pore size and distribution) have been optimised for several decades. However, without major material changes of the starting material, i.e. a-C carbon is still used as basic material.

Objectives

For today's H_2/O_2 GDEs a-C is still the material of choice, using typically *carbon black* as catalyst support and *carbon fibers* as gas diffusion layer (GDL). *Single-*

walled carbon nanotubes (SWNTs) combine properties like high specific surface area, high aspect ratio, high electrical conductivity and porosity. Further, they are chemically stable and mechanically flexible. This allows the entire replacement of regular a-C electrodes by SWNT networks. It will be shown, that these extremely thin and light SWNT GDEs can exhibit comparable performance levels with huge potential for further improvement. In contrast to previous work, the use of a sole carbon material is preferred to simplify the electrode's architecture and preparation.

Functionalization of SWNTs is a central topic of this work. It is a necessary step to transform the intrinsically inert sidewalls and endcaps of SWNTs. The formation of new bonds requires the change of the hybridization of the C-atom leading to local defects (sp^3-defects) in the molecular structure of the SWNTs. The conductivity and spectroscopic studies (*EDX, Raman*) highlight the aspect of oxygen doping on a quantitative level. *Atomic forces microscopy* (AFM) is used for size and morphology/structural analysis of isolated SWNTs and SWNT networks after thermal and sonochemical oxidation varying temperature and duration. *Scanning electron microscopy* (SEM) is done to determine the thickness and porosity of the monolithic SWNT electrodes. *Transmission electron microscopy* (TEM) is used to determine the catalyst size and distribution. Like AFM, SEM and TEM studies are additionally useful for morphology studies.

Outline

The structure and properties of CNTs are outlined in chapter 2. Chapter 3 describes the basic principles of H_2/O_2 fuel cells namely those of *proton exchange fuel cells* (PEFC) and *phosphoric acid fuel cells* (PAFC). SWNT networks are characterized in chapter 4 in their function as extreme thin and light gas diffusion electrodes for H_2/O_2 fuel cells. This includes a short analysis of isolated SWNTs followed by the preparation and characterization of SWNT electrodes including fuel cell testing. Additionally, a first

approach towards electrodes based on aligned *multi-walled carbon nanotubes (MWNT)* is shown in chapter 5 before switching to the conclusions in chapter 6.

2 Carbon nanotubes

2.1 Carbon allotropes

Diamond and *graphite* [7] are the well-known allotropes of carbon. *Fullerenes* and CNTs were just recently discovered [8]. The difference in the structure of these allotropes is responsible for their varying physical properties. The carbon atoms in a diamond are tetrahedrally sp^3 bonded, in graphite they are sp^2 trigonal bonded in hexagonal planes (*graphene layers*). Figure 2.1 displays the structure of different carbon allotropes.

Amorphous carbon (a-C) are graphite related materials with predominantly sp^2 bonding. Among those, carbon fibers and carbon blacks are relevant in today fuel cell technology. *Carbon fibers* exhibit typical diameters of ~10 µm [9] and aspect ratios up to $\sim 10^4$ [10]. They are used for gas diffusion layers and current collector in PEFC/PAFC electrodes. *Carbon blacks* are finely divided carbon particles which are widely used as catalyst support in PEFC/PAFC catalyst layers (e.g. Vulcan XC-72). The microcrystalline structure of these *carbon blacks*, with sizes from 10 to 100 nm [11], lead to aspect ratios close to unity and a specific surface area from ~250 m^2g^{-1} [12,13].

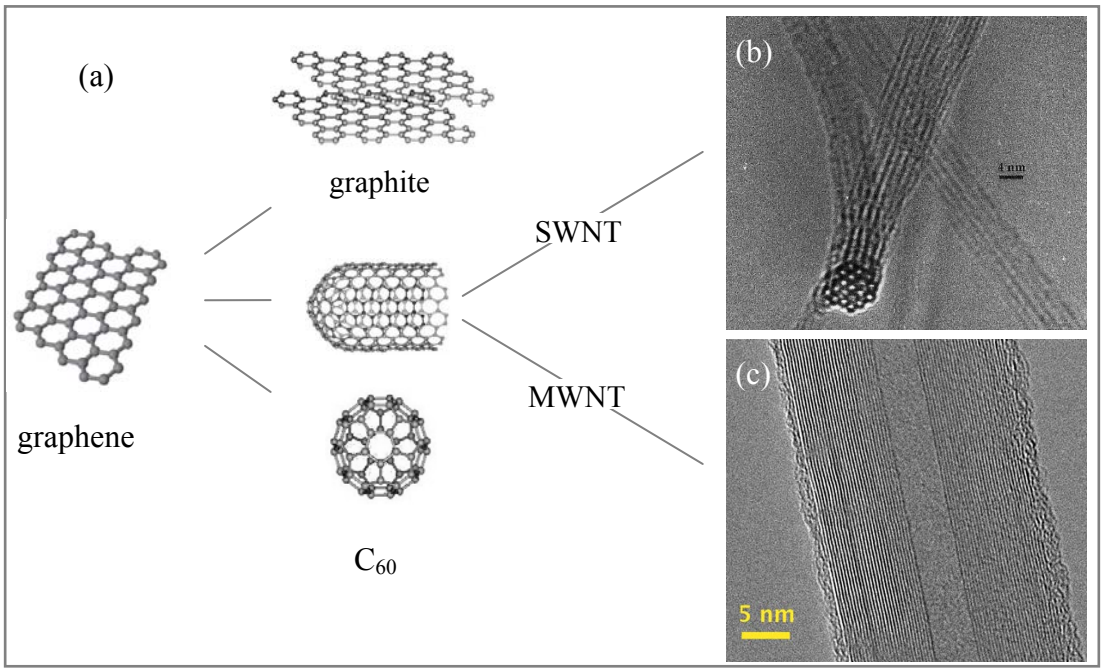

Figure 2.1. (a) Structure of carbon allotropes; (b) Atomic structure of a bundle of single wall carbon nanotubes (SWNTs) (scale 4 nm) [14] and (c) multiwall carbon nanotube (MWNT) [15].

Nanosized fullerenes are spherical molecules with high symmetry containing only hexagonal and pentagonal faces. The most prominent fullerene is the C_{60} molecule [16,17][1]. Cutting fullerenes into two halves connected by a tube leads us to CNTs.

2.2 Structure and notation

The structure of CNTs consists of enrolled graphene sheets (one atomic carbon layers) that can be single- or multiwalled. CNTs consist of two separate interregions with different physical and chemical properties: the sidewall and end caps. The end cap

[1] *From Euler's theorem for polyhedra the smallest possible fullerene is C_{20}, a regular dodecahedron with only 12 pentagonal faces. It is however, energetically unfavorable for two pentagons to be adjacent to each other (so called 'isolated pentagonal rule'). The smallest fullerene satisfying this rule is C_{60}.The C-C bond length of pentagons is 1.46 Å, of hexagons 1.40 Å.*

structure is derived from a smaller fullerene, such as C_{60}. Their diameters range from 0.7 nm (that of C_{60} [18]) to 2 nm for SWNTs and a few tens of nanometers for MWNTs. The length and diameter depend on synthesis conditions and can exceed several hundred μm [16]. The atomic structure of a bundle of aligned SWNTs with a circular section is shown in Figure 2.1b (top). MWNT with its various concentric layers and hallow core by high resolution transmission electron microscopy (HRTEM) is shown also in the bottom of Figure 2.1b (bottom).

Using the notation of *helicity* introduced by Iijima [19], CNTs are defined as *armchair*, *zigzag* and *chiral*, depending on how the graphene sheet is rolled up. Zigzag and armchair tubules exhibit a mirror symmetry plane normal to the tube axis. The classification can be explained in terms of the unit cell and the *chiral vector* $\vec{C}_h$ connecting two crystallographically equivalent sites O and A on a two-dimensional (2D) graphene sheet (Figure 2.2a).

$$\vec{C}_h = n\vec{a}_1 + m\vec{a}_2 \qquad [2.1]$$

CNTs are indexed by two integers (n, m) defining the circumferential length (πd_t), and rolling angle θ of the vector connecting two periodic atom locations as a conceptual graphene sheet 'rolled' into a tube [16].

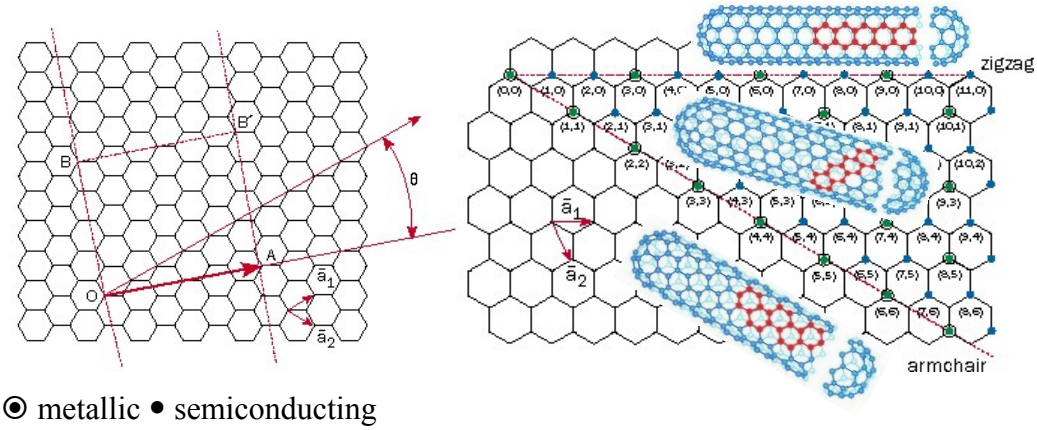

⦿ metallic • semiconducting

Figure 2.2. (a), Rolling vector $\vec{C}_h$ ($O\vec{A}$); (b), SWNT and their symmetries.

CNT's are semiconducting except n-m=3k (metallic) [20]. The 'armchair' (θ=30°) and 'zigzag' (θ=0°) configurations of carbon atoms in planes normal to the tube axis are illustrated in Figure 2.2b. From the indices (n,m) and the nearest-neighbor C-C distance a_{CC}, the nanotube diameter d_t is given by:

$$d_t = \frac{\sqrt{3} \cdot a_{CC}}{\pi} \cdot \sqrt{n^2 + nm + m^2} = \frac{\vec{C}_h}{\pi} \qquad [2.2]$$

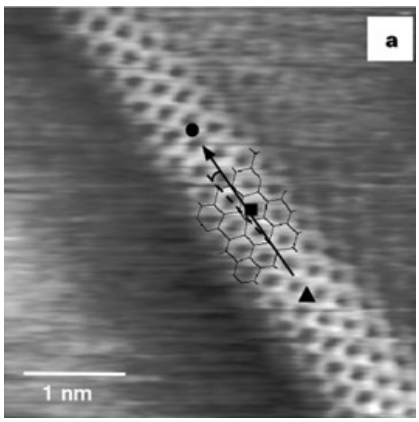

Figure 2.3. Scanning Tunneling Microscopy (STM) image of a SWNT [21].

Figure 2.3 presents a Scanning Tunnelling Microscopy (STM) image of a SWNT to visualize the aspect of chirality. The tube axes are indicated with a solid, black arrow and the zigzag direction are highlighted by dashed lines. A portion of a two-dimensional graphene layer is overlaid to highlight the atomic structure (the symbols have no relevance for this work).

2.3 **Synthesis and properties**

MWNTs were discovered by Iijima [19] in 1991 as a by-product in carbon arc-discharge of fullerene synthesis, two years later Iijima [22] and Bethune [23] independently observed SWNTs. CNTs can be further prepared by *laser ablation* and

chemical vapor deposition (CVD). The tubes are either capped [24] or open [25] during the growth process, the parent vapor grown carbon tube is itself nucleated by a catalytic transition metal particle associated with the adsorption of C_2 dimers [10].

CNTs possess many special properties such as high aspect ratio, electrical conductivity, chemical and mechanical stability and bending flexibility [21,26,27]. The bonding in CNTs is primarily sp^2 with sp^3 bonding in regions of high curvature [16,28].[2] SWNTs are flexible while MWNTs tend to be stiff. SWNTs made by high pressure CO disproportionation (HiPco) with a distribution range from 8-20 Å [29] contain amorphous carbon and Fe particles coated by thin carbon layers. Material synthesized by the HiPco method comprises metallic and semiconducting nanotubes. However, metallic nanotubes do not appear to be particularly strong features in HiPco samples [30] suggesting that HiPco and other synthetic processes may favor the production of armchair and near-armchair nanotubes.

SWNTs self-organize into bundles during growth by van der Waals interactions [31], partly tens of micrometers long. They are remarkably flexible and bend into curved arcs with radii as small as 20 nm [23], being good electrical conductors form long conductive pathways with particularly high aspect ratios leading to surface area of ~1000 m^2g^{-1} [32]. They are poorly soluble in most organic solvents and insoluble in water.

The conductivity of SWNT networks can be varied by the thickness of the material. These changes are thought to be caused by the quantity and the quality of metallic SWNTs included in the mats [33]: non-metallic behaviour in thinner samples (150 nm)

---

[2] *The sp^2 orbitals form strong σ bonds between carbon atoms in the graphite planes while the p_z or π orbitals provide the weak Van de Waals bonds between the planes. The overlap of π orbitals provides the electron bond network responsible for the high electrical conductivity of graphite. In a nanotube each carbon atom is joined to three neighours, so the bonding is essentially sp^2 and small amount of sp^3 character due to curvature. sp^3 results from the mixing of one 2s and three 2p orbitals.*

and metallic in thicker samples (4 μm) according to a simple percolation model [34]. According to their thickness SWNT networks are suitable for thin film transistors [35], transparent electrodes [36] or fuel cell electrode arrays [32,37,38,39,40].

CVD produces MWNTs at moderate temperatures employing the catalytic disproportionation of a carbon containing gas (hydrocarbon molecules, CO) on small metal particles which are supported on inert substrates (e.g. SiO_2). Among the transition metals, iron proved to be an efficient catalyst for CVD production of CNTs. MWNTs are produced e.g., on supported iron catalyst particles with acetylene as feed gas. Acetylene gas flowing over heated sample is decomposed by coated metal particles at temperatures from 700 to 800°C [10]. Plasma enhanced CVD is a means to lower the decomposition temperatures down to 550°C [41].

MWNTs consist of multiple concentric layers with diameters from 10 to 50 nm [42] with an interlayer distance of 3.4 Å [16] and microns of length. MWNTs have a specific surface of 250 to 1000 m^2g^{-1} [43]. MWNTs were recently used as catalyst support [44] and electrodes [45]. The current in MWNTs is mainly confined to the outer layer [42], their large diameter favour low-ohmic contacts. Wang et al. [46] report reduced corrosion in MWNTs compared to Vulcan XC-72.

2.4 **Surface modification**

Surface modification is a necessary step to suspend CNTs, to attach catalyst nanoparticles and to enhance their electric conductivity. *Functionalization* refers to the attachment of chemical groups to alter specific chemical or physical properties. Surface modification of nanotubes using oxidation or reduction lead to functional groups from covalent bonding like CH or CO. Non-covalent bonding is based on Van der Waals or electrostatic forces [47].

The formation of new covalent bonds requires the change in hybridization and leads to local sp^3-defects in the crystal structure of the CNT. The first successful surface modification of SWNTs involved the treatment under oxidizing conditions, such as sonication in mixtures of sulfuric and nitric acid [48]. Functional groups exist primarily at the ends of nanotubes and defect sites along the sidewalls where increased curvature strain results in increased reactivity [49].[3] SWNTs can be separated from each other by sonication in solvents like HNO_3. The HNO_3 treatment introduces large quantities of acidic groups that create a polar surface [50]. The oxidized tubes form small bundles or even remain as individual tubes, which facilitates the coordination of solvent molecules and thus increase solubility [51].

A direct relationship between diameter and reactivity is confirmed. Thereafter smaller tubes diameters are more susceptible to oxidation [52]. Thermal oxidation of SWNTs in air/oxygen occurs at 600 to 700°C [16], of MWNTs at 700 to 800°C [53].

Oxidation results in the formation of functional groups like CO, COOH or COH attached to defects sites and open ends of CNTs [54]. Oxygen-type defects can be introduced by heating in air or oxygen at temperatures above 350°C or treatment with strong acids like HNO_3 or H_2SO_4 [51]. HNO_3 treatment has been reported to increase the surface area for C-HNO_3 [55]. Hiura et al. [56] have shown that the oxidation process covers the surface of nanotubes with carboxylic (-COOH), carbonyl (-CO) and hydroxylic (-COH) groups with a ratio of 4:2:1. Ebbesen et al. [9] have shown that the reactivity of nanotubes is enhanced by pre-oxidation. Mawhinney et al. [57] showed that defects of 5% can be tolerated without loss of the physical properties of SWNTs. Acid purification and cutting processes produce 6–7% oxidized groups [58]. The presence of these carboxylic acids can be further employed for the covalent attachment leading to highly soluble materials. The presence of carboxylate groups is also used to

covalently couple metal particles to defect sites of SWNTs. Direct side-wall functionalization can be achieved by hydrogenation [59]. C-H surface complexes are more stable than C-O surface complexes [60].

Non-covalent functionalization comprises ionic bonding or dipole interaction. In the search for non destructive, non covalent separation and purification methods, it was shown that CNTs can interact with certain molecules such as sodium dodecyl sulfate (SDS, $C_{12}H_{25}SO_4$). [61]. Dissolution in SDS, most common 1% SDS solutions [62], does not require covalent functionalization [29]. The hydrophobic part of the SDS-molecules adsorb on the CNT surface while the ionic, hydrophilic parts assure the solubility in water forming micelles in which the nanotubes are surrounded by hydrophobic moieties.

The electronic properties (carrier density) of CNTs can be changed by *intercalation* or *doping* [63,64,65]. An order of magnitude increase in conductivity can be obtained for many intercalants with the largest increase for strong acid acceptor intercalants [66]. Intercalation compounds are formed by the insertion of atomic or molecular layers of chemical species between the layers of the host material [66]. *Doping* refers to the occupation of random locations with a guest species [7]. The intercalation of nitric acid into graphite is known to be accompanied by hole doping of the graphene sheet [67]. Intercalation can be achieved with solid, liquid or gaseous reactants, while the intercalation rate and resulting intercalate concentration strongly depends on the defect density of the host material [7]. For MWNTs, the guest species can be intercalated between the graphene shells in the same tubes [68,69], intercalants are believed to reside in the open channels between the individual SWNTs inside the bundles [70].

[3] *The pentagon rings are subjected to the largest strain and thus display higher chemical reactivity. In contrast to the open ends and defective sites, sidewalls of the SWNTs posses great chemical stability.*

As in the case of graphite-HNO_3 compounds [71] the intercalant is present in the form of neutral HNO_3 molecules admixed with charged NO_3^- ions. Intercalated $(NO_3^-)(H^+)$ is partially converted to covalently bound $–NO_2$ moieties upon heating [72].

3 The H_2/O_2 fuel cell

3.1 Principle

Fuel cells convert the chemical energy of a fuel directly to electrical energy and heat with the aid of an oxidant. Unlike batteries, they use a continuous supply of fuel from an external storage. The basic components of a H_2/O_2 fuel cell seen in Figure 3.1 are a H_2 and O_2 gas supplying system (1), a positively charged anode (2), a proton conducting electrolyte (3) and a negatively[4] charged cathode (4). 2-3 form together the membrane electrode assembly (MEA).

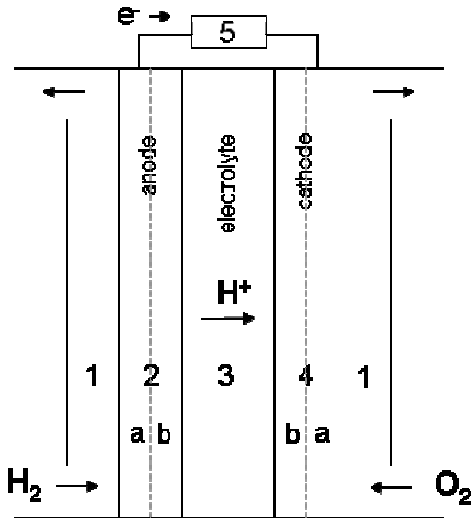

Figure 3.1. Schematic diagram of H_2/O_2 fuel cell.

[4] *Note that the signs of both electrodes are contrary to those in electrolysis because Gibbs free energy in fuel cells is negative ($\Delta G < 0$), see chapter X.*

Gas diffusion [5] is the mode of gas transport in both electrodes. Hydrogen enters the gas channel on the anode side, diffuses through the gas diffusion layer (2a) to the catalyst layer (2b). There, the *electrochemical reactions* take place, hydrogen is catalytically dissociated and oxidized to protons (H^+-ions) and electrons.

$$H_2 \rightarrow 2H^+ + 2e^- \qquad \varphi_{rev\,H2} = 0V \text{ (per definition)} \qquad [3.1]$$

The electron transfer is realized by an external current (5), protons generated from the dissociated hydrogen migrate through the electrolyte to the cathode. Oxygen enters the gas channel on the cathodic side, diffuses through the gas diffusion layer (4a) to the catalyst layer (4b). There, oxygen is dissociated and reduced to O^{2-} ions [73,74].

$$½O_2 + 2H^+ + 2e^- + \rightarrow H_2O \qquad \varphi_{rev\,O2} = 1.23V \qquad [3.2]$$

The latter recombine with protons to water. Thus the principle of the H_2/O_2 fuel cell is the reverse of *water electrolysis*: water is formed catalytically releasing energy in form of electricity and heat.

$$H_2 + ½O_2 + 2e^- \rightarrow H_2O + energy \qquad \varphi_{rev\,H2O} = 1.23V \qquad [3.3]$$

3.2 **Fuel cell types**

Fuel cells exist as low-, mid- (Molten Carbonate Fuel Cells, MCFC) and high temperature fuel cells (Solid Oxide Fuel Cells, SOFC). Alkaline (AFC), Phosphoric Acid -(PAFC) and Polymer Electrolyte (PEFC) operate in the low temperature range.

[5] *According to Justi/Winsel /11/ diffusion can be referred to 'real' volume diffusion or diffusion in gas diffusion electrodes through a pore system.*

Table 3.1. H_2/O_2 fuel cell characteristics [6,75,76].

	AFC	PEFC[6]	PAFC
Temperature	<90°C	<100°C	<220°C
Electrolyte	30 wt% KOH	ionomer	>95% H_3PO_4
Fuel	H_2	H_2	H_2, CH_4
Charge carrier	OH^-	H^+	H^+
Anode catalyst	Ni, Pt	Pt	Pt
Cathode catalyst	Au	Pt	Pt
Efficiency (cell)	60-70%	50-68%	55%
Application	space, submarine	mobile, portable, stationary	mobile, stationary

The electrolyte of a PEFC is a solid proton conducting polymer typically with sulfonated side chains. PEFC membranes like Nafion® from DuPont™ are typically 50-175 μm thick [77]. PAFCs use highly concentrated *ortho-phosphoric acid (H_3PO_4)* fixed in a porous matrix as electrolyte. The cell typically operates at 150 to 220 °C, at lower temperatures phosphoric acid is a poor ionic conductor and CO poisoning of the anodic Pt electrocatalyst is critical (at temperatures higher than 150 °C CO is oxidized to CO_2). The stability of concentrated phosphoric acid is high compared to other common acids with low vapor pressure. A PAFC is CO_2-rejecting, tolerating 1-2% CO at operating temperatures of 150 to 220 °C [6,78]. The protonic chain conduction mechanism utilizes the movement of $H_4PO_4^+$ or $H_2PO_4^-$ ions through a highly hydrogen-bonded structure [79,80]. The electrolyte of the PAFC is composed of silicon carbide (SiC) powder and PTFE binder with thicknesses ranging between 300 μm to 1000 μm [78,81]. Shortcomings are the corrosive electrolyte, H_3PO_4 loss, a stiff

[6] *Direct methanol fuel cells (DMFC) use methanol as the fuel which is catalytically transformed to hydrogen, electrode (Pt/Ru catalyst on anode side) and membrane materials are comparable to those of PEFCs.*

electrolyte matrix, however without the need of humidification and increased CO tolerance

Commercial gas diffusion layers are ~200 to 400 μm thick [81] whereas conventional catalyst layers CL are ~100 μm thick [6]. The latter are made by pressing, rolling or printing mixtures or suspensions of carbon black (Vulcan XC-72) and Pt particles [43]. Vulcan XC-72 acts as the catalyst support with a surface area of ~250 m^2g^{-1} [82,83] and an average particle size of 40 nm [11]. The standard catalyst loading is 0.5mg cm^{-2} (20-30% Pt on Vulcan XC-72) [5,46] with Pt particles of 2 to 5 nm diameter [84,85]. Together with polymeric binders the platinized carbon black particles are supported on carbon fiber based gas diffusion layer. Platinized carbon powders need to be impregnated by a proton exchange polymer electrolyte (typically Nafion solution) before use as PEFC electrodes [86]. However, impregnated Nafion only penetrates about 10 μm into PEFC electrodes [87]]. At temperatures < 80 °C [88,89] CO can easily adsorb on the Pt surface of the fuel cell anode blocking active catalyst sites.

3.3 **Fuel cell characteristics**

3.3.1 Thermodynamics

According to the 2nd law of thermodynamics any reversible process follows

$$\Delta G^0 = \Delta H^0 - T\Delta S^0 \qquad [3.4]$$

with ΔG^0 Gibbs free energy, ΔH^0 the reaction enthalpy and ΔS the entropy. The chemical energy cannot be transformed totally in electrical energy, the amount of $T\Delta S$

(heat exchanged with the surroundings) has to be subtracted. ΔG is directly correlated with the standard electromotrice force (EMF, E^0) of the reaction:[7]

$$\Delta G^0 = -nFE^0 \qquad [3.5]$$

with n the amount of electrons, F the Faraday constant (96,484 C.mol^{-1}). Based on the thermodynamic values in Table 3.2 a maximum reversible potential (E^0) of *1.23 V* per unit cell is possible:

$$E^0 = -\frac{\Delta G^0}{nF} = -\frac{-237\ kJmol^{-1}}{2 \cdot 96485\ Cmol^{-1}} = 1.23V \qquad [3.6]$$

3.3.2 Efficiency

Heat is transformed due to the 2nd law of thermodynamics to mechanical work to a percentage called 'Carnot factor'. The *Carnot efficiency* (η_c) of reversible heat engines is given by the relation (T_1 high- and T_2 low-temperature zone of a combustion engine):

$$\eta_c = \frac{T_1 - T_2}{T_1} \qquad [3.7]$$

Fuel cells are not subjected to the Carnot limitation of thermal machines making them efficient energy converters. Based on eq. [3.4] the ideal efficiency of the fuel cell, the thermodynamic efficiency (η_{th}) is defined as:

$$\eta_{th} = \frac{\Delta G^0}{\Delta H^0} = 1 - \frac{T\Delta S^0}{\Delta H^0} = \frac{nFE^0}{\Delta H^0} \qquad [3.8]$$

[7] *Standard conditions (T=298.15°K/25°C, P_{H2}=P_{O2}=1 atm, H_2O in the liquid state) marked by index ^{0}.*

If the entropy change of the reaction is negative η_{th} decreases with increasing temperature, η_c increases with increasing temperature.

Table 3.2. Thermodynamic data for the H_2/O_2 fuel cell reaction [6,74].

Reaction	ΔG^0 *(kJmol^{-1})*	ΔH^0 *(kJmol^{-1})*	ΔS^0 *(kJK^{-1}mol^{-1})*	*n*	E^0 *(V)*	η_{th}
H_2+ ½ O_2->H_2O (l)	-237	-285	-162	2	1.23	0.83
H_2+ ½ O_2->H_2O (g)	-229	-242	-44	2	1.18	0.95

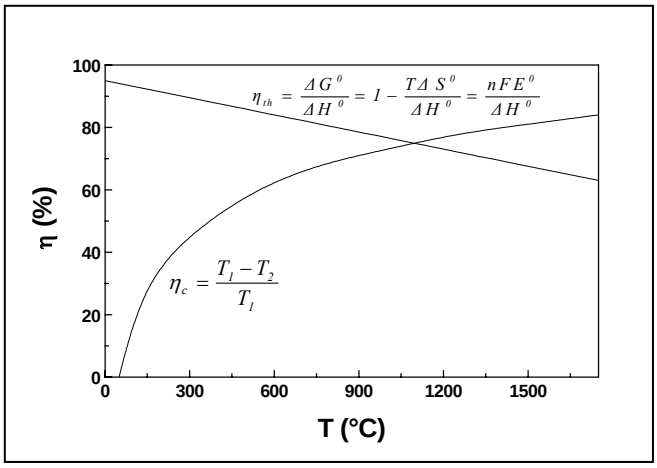

Figure 3.2. Thermodynamic vs Carnot efficiency.

3.3.3 I/U curves

I/U curves are the main characterization method to describe the performance of a fuel cell [78]. The typical form of a I/U curve in a fuel cell is shown in Figure 4.3. Losses

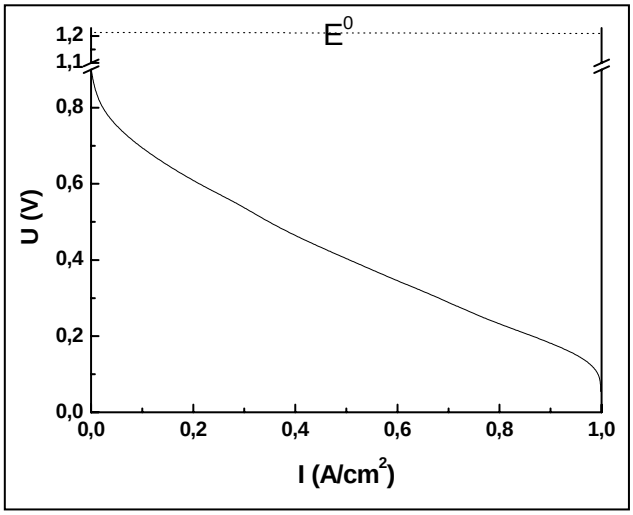

Figure 3.4. I/U characteristic curve of a H_2/O_2 fuel cell.

within the cell are related to *activation polarization* (η_{act}), *ohmic polarization* (η_{Ω}) and *concentration polarization* (η_{conc}) [88], they have an immediate influence on efficiency (Figure 3.2).

The activation loss $\Delta\eta_{act}$ is related to electron transfer at the catalyst/electrolyte interface [5].The kind of catalyst, electrode area and operating temperature have a direct influence on activation polarization given by (a,b as integers, i current density[8]):

$$\eta_{act} = a + b \ln i \qquad [3.9]$$

Ohmic polarization η_{Ω} is caused by resistance (R) in the cell and can be reduced by using components with high ionic conductivity and by reducing the membrane thickness.

[8] *The term b is called the Tafel slope, and is obtained from the slope of a plot of* η_{act} *as a function of log i.*

Concentration polarization η_{conc} results from energy losses associated with mass transport, including transporting process gases, removing product water and impurities from the reaction sites:

$$\eta_{conc} = \left(\frac{RT}{nF}\right) ln(1 - \frac{i}{i_L}) \qquad [3.10]$$

The limiting current (i_L) Fick's first law of diffusion [14] can be derived from

$$i_L = \frac{nF \cdot D\, A\, c_g}{\delta} \qquad [3.11]$$

with D the diffusion coefficient, A the specific surface area, c_g the concentration of the dissolved gas and δ the thickness of the diffusion layer.

3.4 Three-phase zone

Electrochemical reactions in a fuel cell take place at the *Three-phase zone* (TPZ), the conjunction of electrode catalyst, reactant gas and electrolyte. A major part of the TPZ belongs to the catalyst. To date, platinum has proven to be the best catalyst for hydrogen oxidation and oxygen reduction [90]. Activated carbon (typically Vulcan XC-72) is the most common support material for electrocatalysis. Peuckert et al. [91] showed that the best activity of the oxygen reduction reaction, the limiting reaction of the fuel cell, occurs for particles of diameters from 3 to 4 nm. Below 3 nm diameter the activity of platinum is reduced, attributed to a decrease in the number of catalyst sites with adequate coordination number [92]. With 5 nm Pt particles the activity drops to 85%, for 1.4 nm sized particles to 33% [93]. For the oxygen reduction, a loss of catalytic activity with decreased Pt particle size is confirmed experimentally [94], correlated to a stronger adsorption of oxygenated species during the oxygen reduction. Thin electrocatalyst layers are favourable to minimize mass transport and ohmic limitations that predominate at high current densities [87]. At the same time the

catalyst utilization in commercial fuel cells is low with 20-30% [95], mainly due to inaccessibility to the reactant sites and large Pt particles [96].

For low overpotentials and high current densities a maximum of the catalyst clusters need to be integrated into the electrolyte network [97]. Localization of Pt in vicinity of the electrolyte has been known to exhibit higher fuel cell performance [98]. Sputtered platinum directly on Nafion membranes shows comparable performance to standard electrodes [99,100]. Heterogeneous Pt/C catalysts can be prepared by the chemical or electrochemical reduction of Pt salts (e.g. H_2PtCl_6, K_2PtCl_6). Standard electrodes are made from platinum black [101] deposited on carbon black. Alternatively, Pt salt solutions can be brushed or printed onto the electrodes and then reduced to active catalysts [102].

The electrolyte has to separate the feed gases (H_2/O_2) and to ensure the proton transport between the two electrodes. Hydrogen bonding is considered a prerequisite for proton conduction [103]. Two mechanisms of proton transfer are mainly in discussion: the 'vehicle mechanism' where the proton is supported by a solvated, bigger species (e.g. H_3O^+) and the Grotthus mechanism which involves a correlated proton jump between host molecule and correlated reorientation of the latter. Most proton conductors rely on water to maintain their conductivity [104], only a few materials offer high proton conductivity and sufficient chemical stability between 100-200°C, e.g. phosphoric acid.

The electrolyte has to be impermeable for gases and highly conductive for protons. Phosporic acid was introduced into fuel cell technology because it is stable at high temperatures allowing good performance at temperature above 190 °C at P = 1 atm [73]. For use in fuel cells the electrical conductivity of the anode (cathode) has to be of the order of 10^2-10^3 S/cm to keep the ohmic loss much lower than the ohmic loss of H^+-conducting membrane (H_3PO_4, Nafion® 117: $\sigma \sim 10^{-1}$ S/cm at T = 80 °C [73]). The

influence of temperature on the solubility (c_{O_2}) and diffusivity (D_{O_2}) of oxygen in highly concentrated H_3PO_4 are in Table 3.3.

Table 3.3. Solubility and diffusivity of oxygen in 98% H_3PO_4 [73].

T (°C)	*10^6 (c_{O_2})* *mol/cm^3*	*10^6 (D_{O_2})* *cm/s*
25	0.0494	1.18
75	0.0918	6.28
150	0.107	29.9

4 The SWNT electrode

4.1 Sample preparation

The as-received purified SWNT raw material from *CNI*® [105] was mixed with 65% HNO_3 and treated with a tip sonicator. The power was set to 100W, applied with one-second pulses. The duration of the ultrasound treatment varied from 1 to 60 minutes producing SWNTs of different oxidation levels and with different amount of functional groups. Half of the sonicated SWNT solution was mixed with 60 wt% PTFE dispersion in water (*Sigma-Aldrich*® [106]) to a ratio of 4:6. Afterwards, the solution was filtered (Figure 4.1a) through a 0.1 μm pore sized filter membrane from *Osmonics*® [107] using a simple filter flask at moderate vacuum ($p = 10^{-1}$ atm).

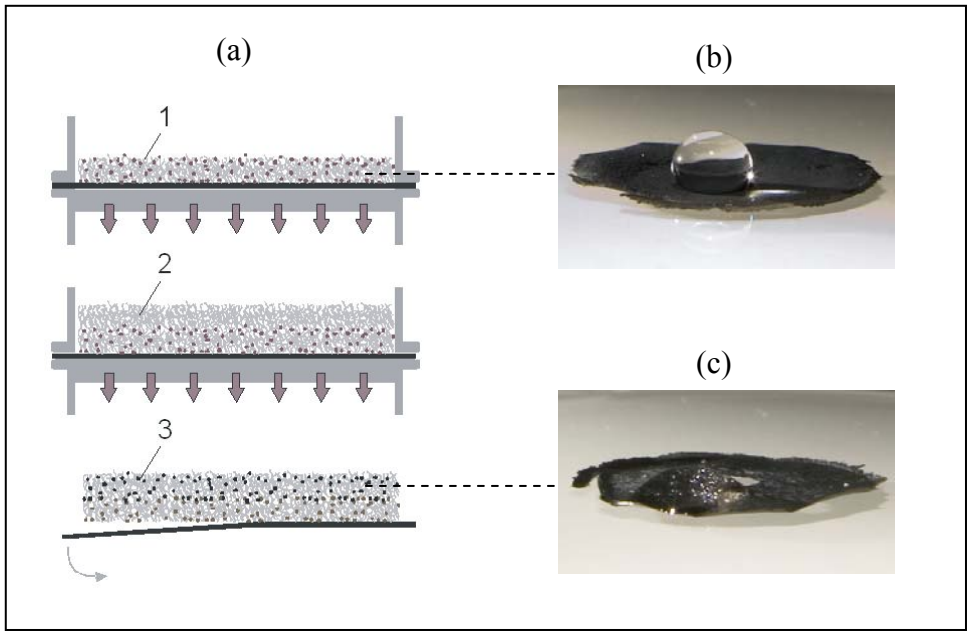

Figure 4.1. (a), Preparation steps of SWNT electrode with varying wettability; (b), GDL; and (c), CL.

SWNTs and PTFE particles remained on the filter forming an entangled hydrophobic network serving as the hydrophobic part of the SWNT electrode (Figure 4.1.a1). The rest of the SWNT solution was cast on top of the PTFE functionalized SWNT network leading to a hydrophilic top layer (Figure. 4.1.a2). The filter cake (bucky paper) was purified thoroughly with conc. hydrochloric acid (HCl) and distilled water. Afterwards a solution of hexachloroplatinate (IV) /isopropanol (0.1 M H_2PtCl_6) was cast on top of the hydrophilic side. After evaporation of isopropanol at RT for 1/2 h the dry SWNT network was annealed at 100 ° C under H_2 flow for 1 h to reduce the precursor salt to metallic Pt catalyst particles As a last step the double layered SWNT network was removed from the filter membrane (Figure 4.1.a3) providing a freestanding electrode. For fuel cell testing anode and cathode were prepared in the same way.

Surface modification by ultrasound treatment of the SWNTs in nitric acid improved the wetting characteristics prior to metal nanoparticle deposition. The higher wettability of the CL (Figure 4.1.c) with $\theta_c << 90°$compared to the GDL (Figure 4.1.b) is obvious. The almost complete wetting can be explained with the polar SWNT network without any PTFE admixture.

Using PTFE the wetting behaviour can be tuned hydrophobic as demonstrated in Figure 4.1.b by the water droplet test. It is obvious from the contact angle that the SWNT network exhibits hydrophobic behaviour. The contact angle of the water droplet in Figure 4.1.b is in good agreement with that given in [108]. The non-polar, chemically inert and hydrophobic nature of the CNT/PTFE surface provides an ideal adjustment to prevent fuel cell flooding. The degree of hydrophobicity was tuned by the amount of PTFE and the annealing temperature (up to 300°C), while the PTFE penetration distance into porous materials is thought to increase linearly with the square root of the annealing time [109].

4.2 Atomic forces microscopy

Atomic forces microscopy (AFM) [110] allows a quick insight into the surface morphology.

Prof. Dr. Enrique Fatás Lahoz Prof. Dr. Enrique Fatás Lahoz

4.2.1 Isolated SWNT

The smallest entity of SWNT electrodes refers to isolated SWNTs. The AFM image in Figure 4.2.a gives an impression of the size dimension of such a SWNT, with several microns in length. The section analysis in Figure 4.2.b reveals a tube diameter of 1.43 nm which is in good agreement with [111] showing the beneficial effect of high aspect ratios and high specific surface area of SWNTs.

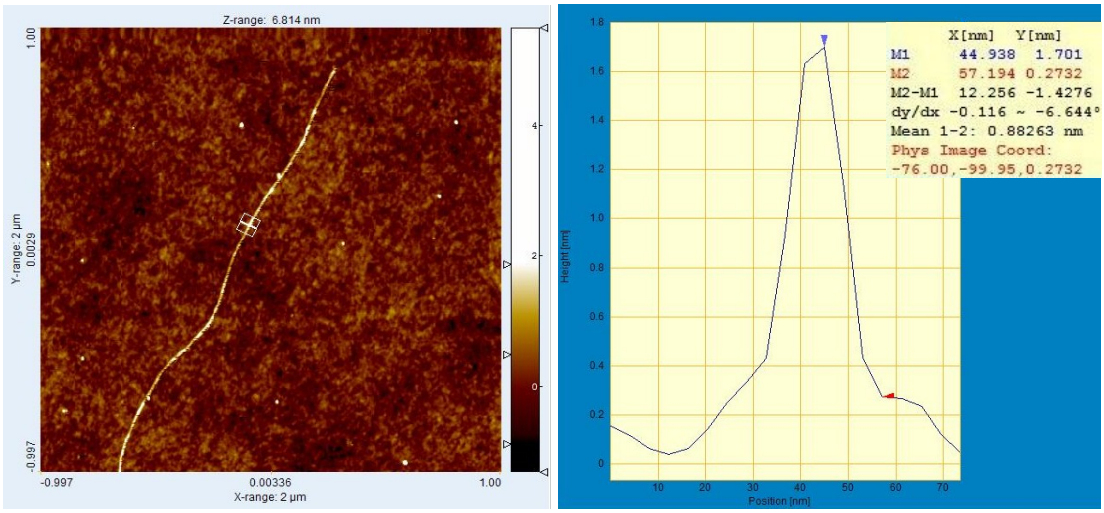

Figure 4.2. (a), AFM image of an isolated SWNT. The white square was taken for analysis. (b), section analysis.

Since electrodes in H_2/O_2 fuel cells are exposed to elevated temperatures their thermal resistance is crucial. In the following SWNTs of different growth catalysts are compared with respect to their thermal resistance. SWNTs were heated in air either

gradually (in 20 to 50 °C steps, typically for 20 min) or exposed to a certain set temperature. SWNTs made from arc discharge (NiY catalyst) were heated gradually to 450 °C (Figure 4.3). The tube shown in Figure 4.3a at 425 °C (arrows for guideline) disappears afterwards at 450 °C (Figure 4.3b).

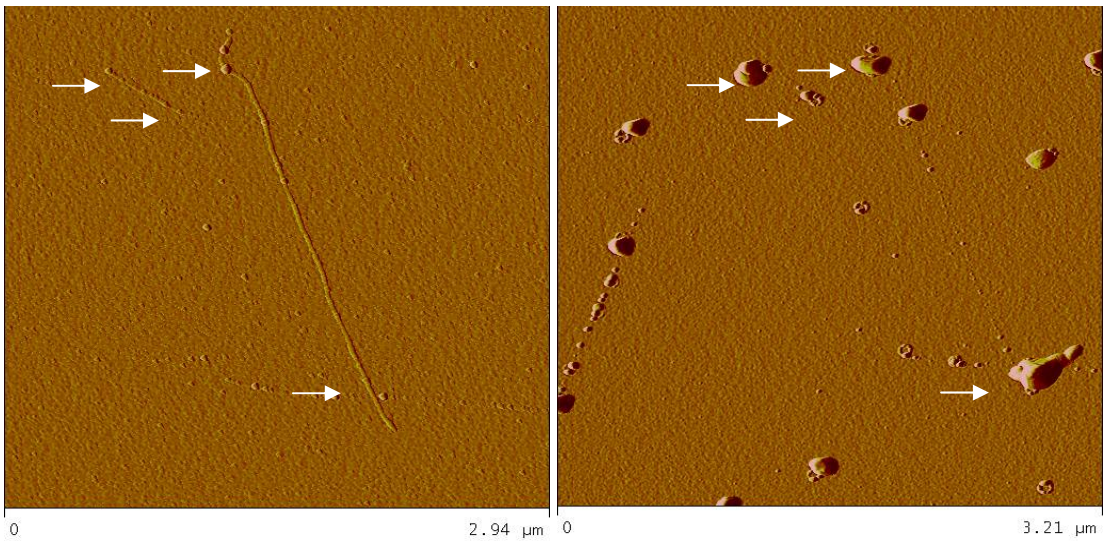

Figure 4.3. SWNT (NiY catalyst) at: (a), 425 °C; and (b), 450 °C (gradual heating).

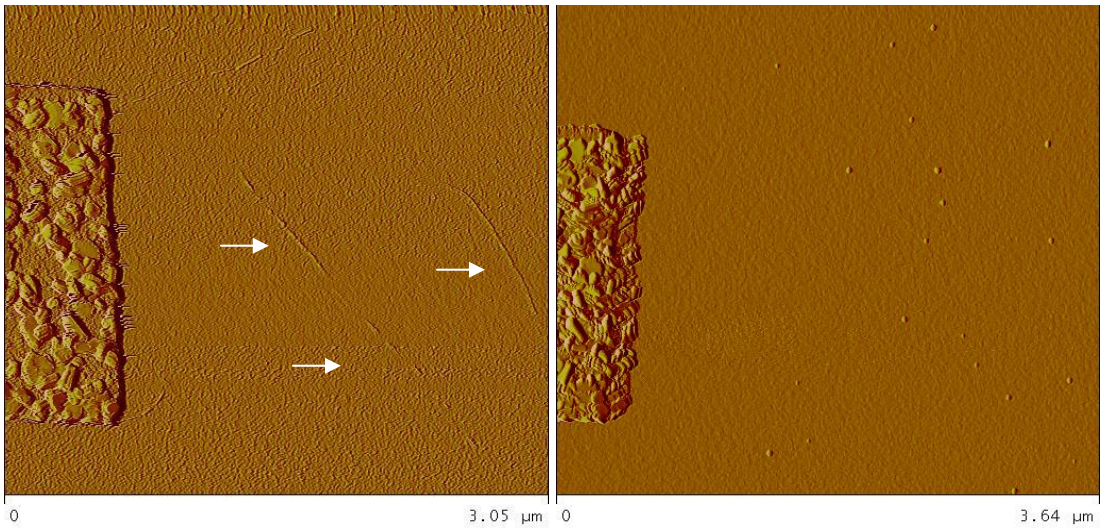

Figure 4.3. SWNTs (NiY catalyst) at: (a), 380 °C; and (b), heated twice at 380 °C.

Heating of a comparable SWNT damages the tube already at 380 °C (Figure 4.3a). When heating the sample twice (at 380 °C) the tubes disappear completely (Figure 4.3b).

By using SWNTs made by CVD (with iron as catalyst) the tube withstands higher temperatures when gradually heated (Figure 4.4). A comparison between room temperature (Figure 4.4a) and 470 °C (Figure 4.4b) shows no visible changes of the tube.

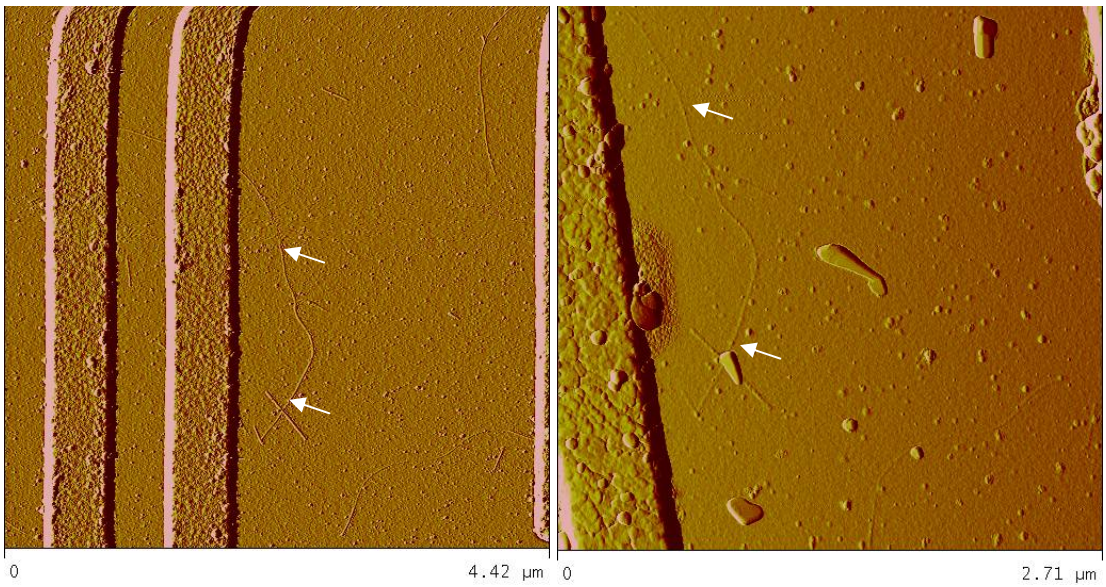

Figure 4.4. SWNT (Fe catalyst) at: (a), room temperature; and (b), 470 °C (gradual heating).

The following SWNTs made with non-magnetic catalyst (Pt/Rh/S) [112] are shown in Figure 4.5. Opening of the tube ends is reported at 400 °C [111]. The SWNT attached to the silane marker (inverse triangle in Figure 4.5a) are burned completely at 550 °C (Figure 4.5b).

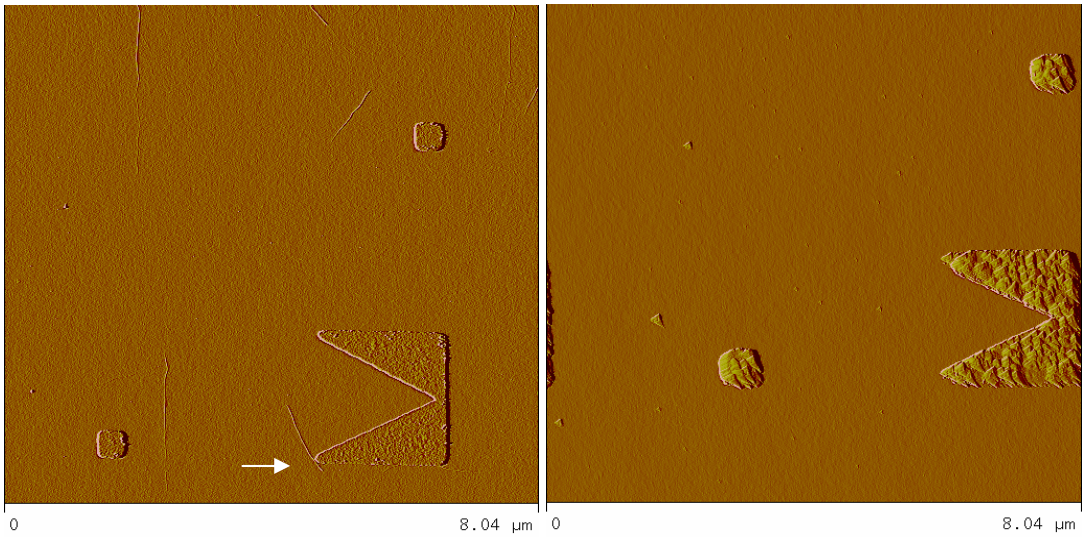

Figure 4.5. SWNT (Pt/Rh/S catalyst) at: (a), room temperature; and (b), 550 °C.

The highest temperatures were achieved by gradual heating (Figure 4.6a) of the tubes made with non-magnetic catalyst (Pt/Rh/S). The SWNT is clearly visible in spite of the advanced surface erosion (Figure 4.6b).

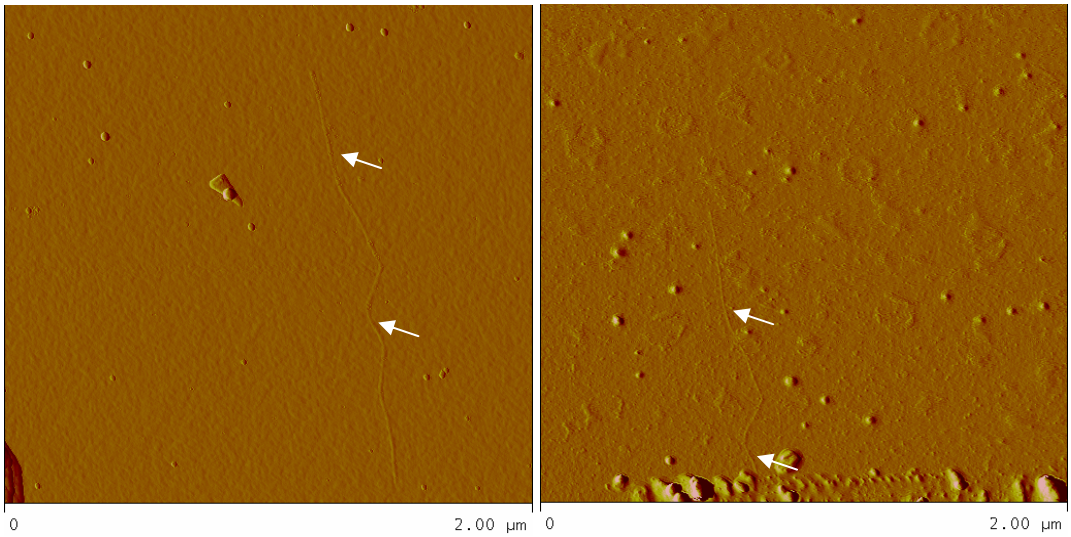

Figure 4.6. SWNT (Pt/Rh/S catalyst) at: (a), 650 °C; and (b), 700 °C (gradual heating).

Table 4.1 summarizes the temperature behaviour of the SWNTs relative to the growth catalyst. Tubes grown by precious catalysts (Pt/Rh/S) withstand the highest temperatures. Gradual heating is a means to expose SWNTs to higher temperatures. Hence, SWNTs can withstand the temperatures common in H_2/O_2 fuel cells (<220 °C).

Table 4.1. Thermal resistance of isolated SWNTs.

	T (°C)	T (°C) gradual heating
Arc discharge (NiY)	380 (burned)	425
CVD (Fe)	_	470
Arc discharge (Pt/Rh/S)	550 (burned)	700

4.2.2 SWNT networks

The electronic properties of SWNT networks vary with their morphology and thickness. Very thin SWNT networks (<< 1µm) exhibit semiconducting properties which makes them a promising material for thin film transistors [113,114,115]. Non-transparent, dense SWNT networks (> 1µm) have the potential to replace a-C as electrode material in electrochemical devices such as double-layer capacitors [116,117] and batteries [118,119]. Such dense SWNT networks ('buckypapers' or 'mats') are shown in Figure 4.7 and Figure 4.8. In those networks the SWNTs are normally bundled. Compared to a-C, SWNT networks offer higher surface area and porosity. Thus they fulfil the requirements to act at the same time as catalyst support and GDL. This way, the a-C electrode can be entirely replaced by a SWNT network. As a major advantage this simplifies the architecture allowing the manufacturing of extremely thin and light gas diffusion electrodes with a minimum of material.

The SWNTs were functionalized by sonochemistry, i.e. time-controlled oxidation (ultrasonication in HNO_3, US/HNO_3) was used to introduce different amounts of functional groups. The AFM images of SWNT networks were recorded after 3 and 5

minutes (Figure 4.7.a and Figure 4.7.b, respectively) as well as 30 and 60 minutes (Figures 4.8.a and Figure 4.8.a, respectively) of US/HNO_3 treatment.

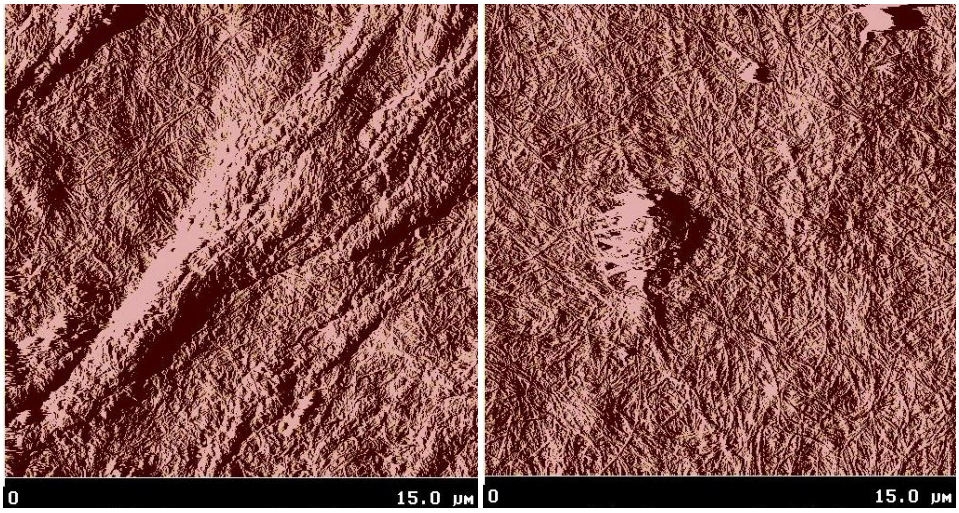

Figure 4.7. AFM images of SWNT networks after sonication in concentrated HNO_3 for: (a), 3 min; and (b), 5 min.

The AFM images demonstrate a debundling within the first minutes (compare figures for 3 min and 5 min, respectively). The effect of partial exfoliation of SWNT bundles is known to occur during purification procedures with HNO_3 [70,120]. The debundling might contribute to the increased conductivity as well (see next chapter), due to an increased number of conducting paths [121]. The tube length decreased starting with 2-10 µm for short sonication (3-5 min) to less than 1 µm (60 min). Both the break down of the SWNT structure and the decreasing SWNT length [122] lower the conductivity of the SWNT network significantly.

For longer US/HNO_3 treatments, however, the continuous oxidation leads to a disordered structure and to an increasing formation and accumulation of amorphous carbon. The initial structure starts to disappear after 30 min (Figure 5.8.a) and is almost completely erased after 60 min (Figure 5.8.b).

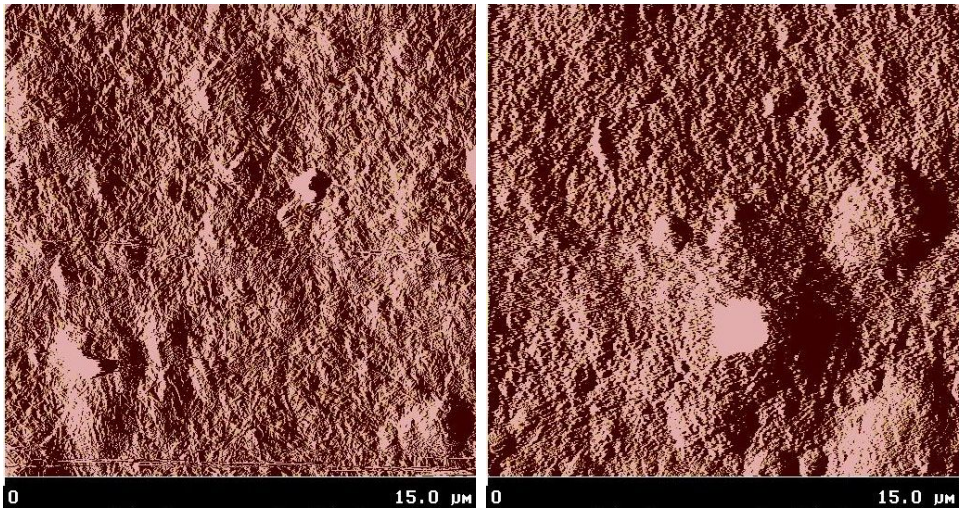

Figure 4.8. AFM images of SWNT networks after sonication in concentrated HNO_3 for: (a), 30 min; and (b), 60 min.

4.3 **Conductivity**

Four-point electric resistance measurements are usually applied to determine the conductivity of CNT networks [20,123] and fuel cell electrodes [66]. The *conductivity* (κ) of a sample is given by:

$$\kappa = \frac{l}{R\,A} \qquad [4.1]$$

with l the length of the sample, R the resistance and A the cross sectional area. Four-probe resistance measurements were recorded at room temperature. The influence of electrode thickness and mode of preparation on conductivity can be seen in Figure 4.9. SWNTs sonicated in HNO_3 offered a magnitude higher conductivity. A maximum conductivity is reached after 3 minutes of sonication. For longer treatment, the conductivity decreases again and falls below the initial value. The observed behaviour can be understood as a trade-off between increasing doping of SWNTs and increasing

scattering when functional groups are introduced by sonication. This way, one can divide the entire process into two parts: doping within the first few minutes (here 3 minutes) and a breakdown of the structure.

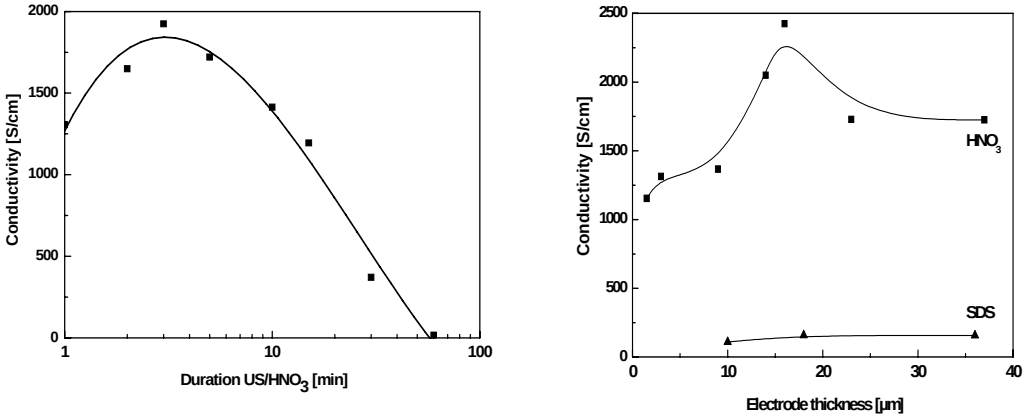

Figure 4.9. Influence of: (a), sonication time; and (b), electrode thickness on conductivity.

The advantages of using SWNT networks for fuel cell electrodes become obvious when its basic properties such as conductivity σ, thickness d and weight m are directly compared to a commercially available a-C electrode (Table 4.2). The conductivity is improved by more than two orders of magnitude whereas thickness and mass are decreased by more than one order of magnitude. Therefore, extremely thin and light gas diffusion electrodes can be realized when using SWNT networks. The best performance with 2,425 S/cm was achieved with an electrode thickness of 16 µm and a weighted sample of 1.5 mg/cm^2 (1g/cm^3).

For comparison, SWNT suspensions using 1% sodium dodecyl sulfate (SDS) as surfactant (with a constant ratio of 1 mg SWNT to 1 ml solvent) were also prepared using the same tip sonicator and filtration. The SDS treated samples did not exceed 159 S/cm. Comparable values are given in [29] with 155 S/cm indicating possibly the isolating effect of the surfactant SDS. The dependence of sonication time on

conductivity is shown in Figure 4.10. A maximum of 1,925 S/cm is reached after 3 min, holding the load throughout at 0.5 mg SWNT/cm^2.

Table 4.2. Physical properties of various GDEs.

	σ *(S/cm)*	*thickness (µm)*	*carbon load (mg/cm²)*	*density (mg/cm³)*
E-TEK [84]	0,8 ±10%	410 ±60	23 ±0.5	561
	2425	16	1.5	938
SWNT/Pt (HNO_3)	2049	14	1.0	714
	1368	9	0.5	556
	158	36	1.5	417
SWNT/Pt (SDS)	159	18	1.0	556
	110	10	0.5	500

Compared to commercial E-TEK electrodes which have conductivities of ~1 S/cm and thicknesses of ~400 µm [84] the SWNT electrodes are superior. In terms of weight the SWNT electrodes have a carbon load of ~1 mg/cm^2 in contrast to ~23 mg/cm^2 of E-TEK electrodes [84]. The electrodes were neither pressed nor sintered at about 300°C as proposed e.g. by Kordesch [102]. Moderate pressing is known to increase the conductivity by improving the rope-rope contacts [20,124].

4.4 Spectroscopy

4.4.1 EDX

Samples were investigated by *energy dispersive X-ray spectroscopy* (EDX) to estimate the quantity of functional groups. It is assumed that the concentration of physisorbed oxygen on the CNT surface is independent of the number of functional groups [125]. The introduction of covalently bonded oxygen defects leads to a change of the ratio of

carbon and oxygen atoms ($r_{O/C}$). Using EDX, the expected change of $r_{O/C}$ as function of sonication time can be analyzed and is presented in Figure 4.11.

The elemental analysis of SWNTs as indicated in Table 4.3 shows a significant enhancement in oxygen and platinum content relative to ultrasound exposure in HNO_3. While the metal content is reduced as would be expected for acid treated material, the elemental analysis also indicates a significant increase in oxygen with increasing sonication. This is due both to the incorporation of oxygen atoms into the nanotubes (e.g. in the form of COOH groups) as well as to the presence of additional surfactant [72].

Table 4.3. EDX composition of SWNT/Pt electrodes.

Sonication time (min)	*Content of elements (wt%)*					*Pt load ($\mu g/cm^2$)*
	C	O	Cl	Fe	Pt	
3	64.6	4.0	3.1	7.8	20.5	317.3
10	63.7	4.2	2.1	3.5	26.6	417.6
30	54.1	7.7	1.7	1.3	35.2	650.6

SWNTs still contain appreciable amounts of contaminants like iron and chloride. They may form oxygenated species that contribute to CO oxidation by lowering the potentials for the onset of CO oxidation [72]. US/HNO_3 is a means to decrease the amount of iron (growth catalyst) and chlorine (catalyst solution), a purification effect e.g. applied in [126].

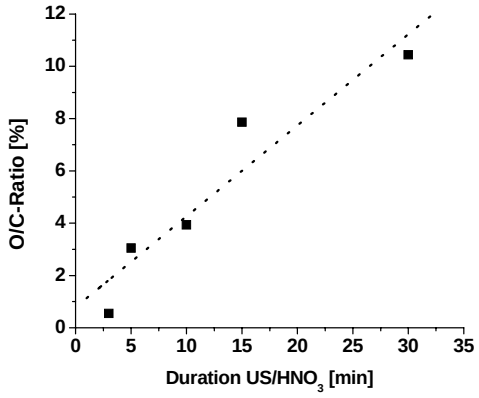

Figure 4.11. (a), Change of the atom ratio between oxygen and carbon ($r_{O/C}$) upon US/HNO_3-treatment; and (b), dependence of the Raman shift on the oxidation oxidation level for the D* modes.

The linear dependence is in agreement with the results of Xing et al. [125] for MWNTs. In their work, an expected saturation of the oxygen content (~5 atom%) has not been observed before 2 h of sonication. Considering that the maximum conductivity has been reached after 3 min (Figure 4.11), one may define $r_{O/C}$ 2% as sufficiently high to determine the properties of SWNT networks.

4.4.2 Raman

Since the discovery of CNTs, *Raman spectroscopy* (RS) has been used to characterize the physical properties of CNTs like nanotube structure and electronic properties [2]. RS also provides information about the concentration of defects and functionalization (doping). The main features in the Raman spectra of SWNTs are the diameter-dependent radial breathing mode (RBM, ω_r) at 100 to 500 cm^{-1} [127], the disorder (D) mode at 1350 cm^{-1} with the corresponding second order peak around 2700 cm^{-1} (D*), the tangential graphite mode (G-mode, TM, ω_t) at 1582 cm^{-1} and its second order peak around at 3160 cm^{-1} (G*):

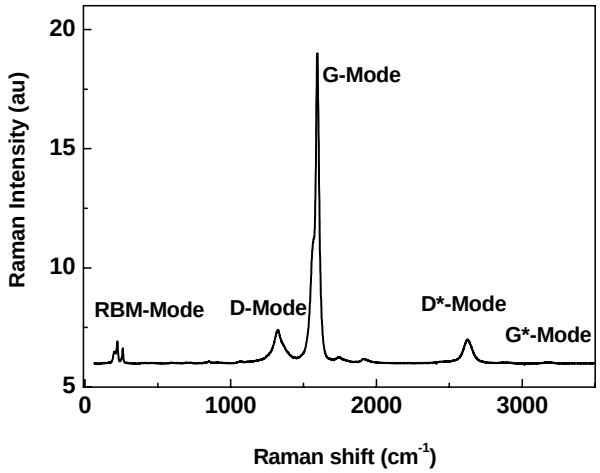

Figure 4.12. Characteristic Raman bands of a HiPco- SWNT sample.

The RBM and the G band are due to a first-order resonance Raman process. In the RBM the C atoms are vibrating in the radial direction with the same phase, in the G mode tangentially against each other [66]. The RBM is directly related to the diameter of the tubes by the relationship [2]:

$$\omega_r = \frac{C_1}{d_t} + C_2 \qquad [4.2]$$

with ω_r the breathing mode in wavenumbers, d_t the diameter of a given tube in nanometers, C_1 = 223.5 cm^{-1} and C_2 = 12.5 cm^{-1} (experimentally determined parameters for HiPco samples [128]). The G band accounts for 3 to 6 Raman allowed modes appearing in the frequency region 1500–1600 cm^{-1}.

The D band[9] is the most studied disorder-induced feature in SWNTs and other carbon-based materials. The D mode is diagnostic of disruptions in the hexagonal CNT

[9] *The double-resonance Raman scattering process involves light absorption, scattering by a phonon, scattering by another phonon (combination mode) or by a defect as in the case of the D band and light emission*.

framework like sidewall defects and open tube ends as well as of impurities like amorphous carbon introduced during growth [129]. The degree of graphitization can be characterized by the ratio I_D/I_G. Purer samples correspond to lower I_D/I_G ratios and sharper first and second order D and G peaks [130]. The spectra of amorphous carbon (a-C), graphite powder, single-crystal graphite and carbon fibres are included due to their presence in commercial electrodes (Figure 4.13). The single sharp lines at 1332 cm^{-1} of diamond and of the C_{60}-fullerene are also illustrated:

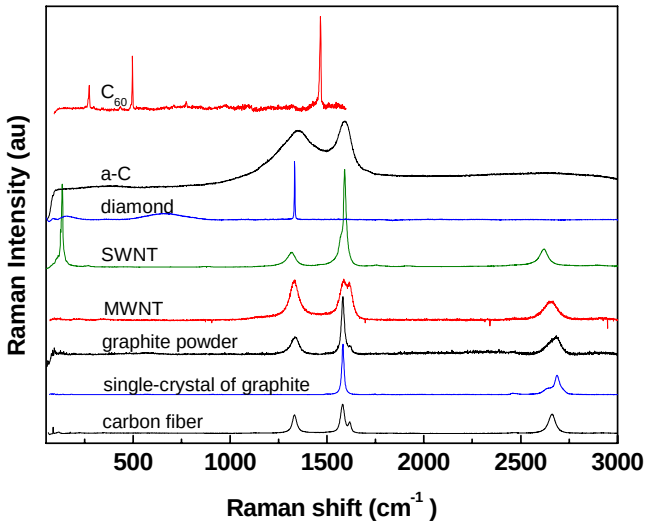

Figure 4.13. Raman spectra of different carbon allotropes [131].

Most of the characteristic differences that distinguish the Raman spectra in carbon nanotubes from those of graphite do not exist for MWNTs because of the larger diameter of the outer tubes. This makes it difficult to distinguish the Raman signal of MWNTs from that of thin graphite fibers.

Raman experiments indicate that acceptor dopants like HNO_3 cause the in-plane graphite layers to contract as electrons are removed [66]. The related frequency upshift in the Raman peak position in oxidized SWNT films is due to the positive charge on the nanotubes produced by the charge transfer reaction with the residual nitric acid.

Upon heat treatment at 350 °C, the initial tangential stretching mode frequency of the film can be recovered [132]. Ionic-acceptor doping of SWNT networks causes an increase of electrical conductivity that correlates with an increase in the frequency of Raman spectral lines [133].

Figure 4.14 illustrates the Raman spectra of SWNT samples after ultrasound/HNO_3 (US/HNO_3). All Raman spectra were recorded at room temperature with a He-Ne laser and an excitation wavelength of λ = 633 nm (1.96 eV). It is obvious that the intensity of the D-Mode increases with increasing US/HNO_3 treatment. In the following, RBM, D and G-mode are examined in detail.

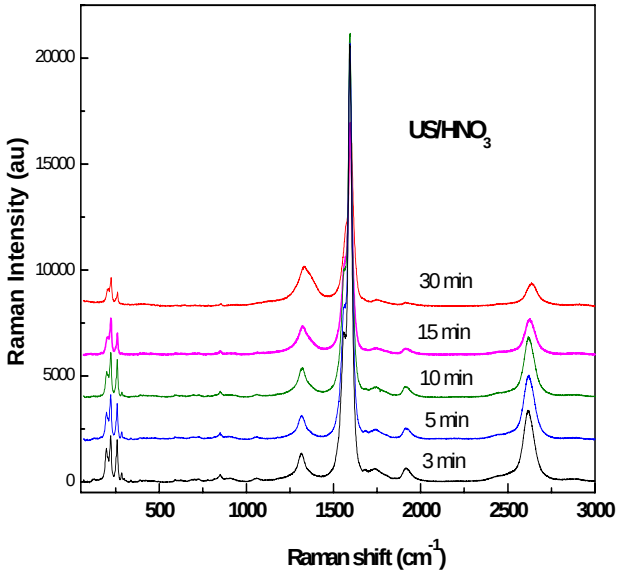

Figue 4.14.As measured Raman spectra of SWNTs after US/HNO_3 treatment.

All RBM modes lost intensity through the sonication in concentrated HNO_3, see also [134]:

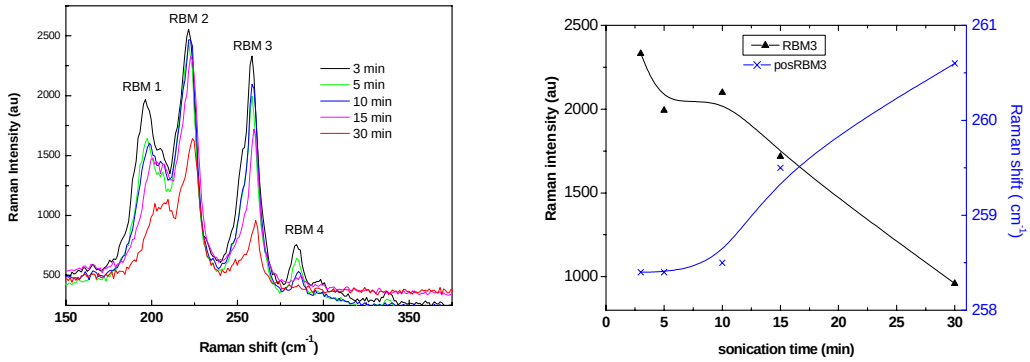

Figure 4.15. (a), RBM spectra of a sonicated SWNTs in 69% HNO_3; (b), Raman intensities and shift of RBM3.

The four RBM modes in Figure 4.15.a exhibit an upshift of the Raman f with increased oxidation while the RBM intensity decreased with sonication time. This trend is illustrated for RBM3 (Figure 4.15.b). The correlation between Raman shift and electrical conductivity observed by [133] is consistent with the measured data. The RBM frequencies range from 196 to 287 cm^{-1} which corresponds to a diameter distribution from 0.9 to 1.3 nm, comparable to the value reported in [129].

Table 4.4. RBM shifts dependent on sonication time in concentrated HNO_3.

Sonication time (min)	*RBM1 (cm^{-1})*	*RBM2*	*RBM3*	*RBM4*
3	196.4	221.1	258.4	284.4
5	197.5	222.2	258.4	284.6
10	198.6	222.4	258.5	285.5
15	200.7	222.3	259.5	287.2
30	201.9	223.7	260.6	-

The strongest upshift is that of the first mode (RBM1) which arises from the SWNTs with the largest tube diameter. The upshift of RBM1 and RBM4 are stronger than those of RBM2 and RBM3. After 30 min the RBM4 diminished in intensity completely.

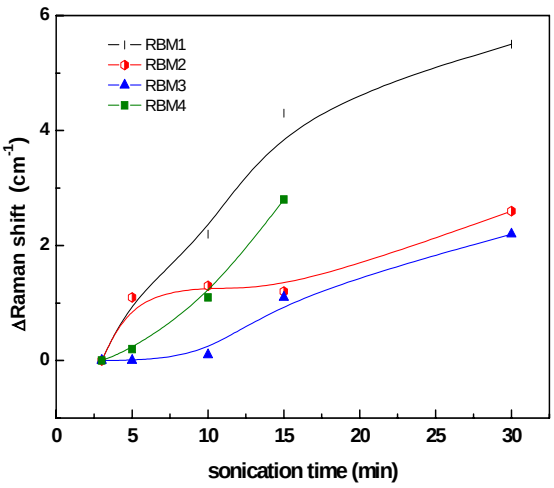

Figure 4.16. Raman shift of the RBM modes (Δ referenced to 3 min, see Table 4.4).

The strong increase of the RBM1 mode with oxidation may be explained with a stronger functionalization of the tube surface. Additionally, a larger intertube channel space might allow an increased penetration of the oxidant. For the smallest tubes, the curvature dependent higher reactivity may explain the stronger shift of RBM4.

On heat treatment using the laser excitation wavelength of 633 nm, the dopant effect is minimized or eliminated, resulting in stronger Raman scattering intensity [132]. Laser annealing of SWNT films is roughly equivalent to thermal annealing to a temperature of about 590 °C (with a 514 nm laser) [72]. After 10 min local heating under ambient conditions the RBM peak increased strongly (Figure 4.17.a). With further heating (20 min local heating), the RBM signal decreased but was still higher than that of the non-

heated sample. It is assumed that some of the SWNTs undergo healing during the annealing process [129].

The SDS treated sample (Figure 4.17.b) shows almost identical RBM spectral lines after first and second heating, the intensities are clearly higher than those treated with HNO_3.

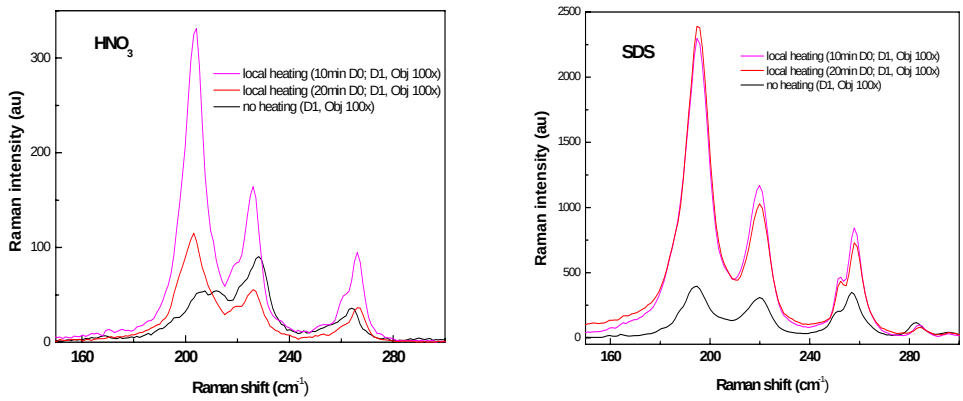

Figure 4.17. Heating effects on RBM Raman spectrum of SWNTs treated with: (a), HNO_3; and (b), SDS.

The Raman spectra of Figure 4.18 show increase in the relative intensity of the disorder mode upon oxidation, characteristic of the introduction of defects [48], the frequency uphift is strong, the D peak broadens. Similar results could be observed for the G-mode in Figure 4.19 a decrease in Raman intensity and frequency upshift.

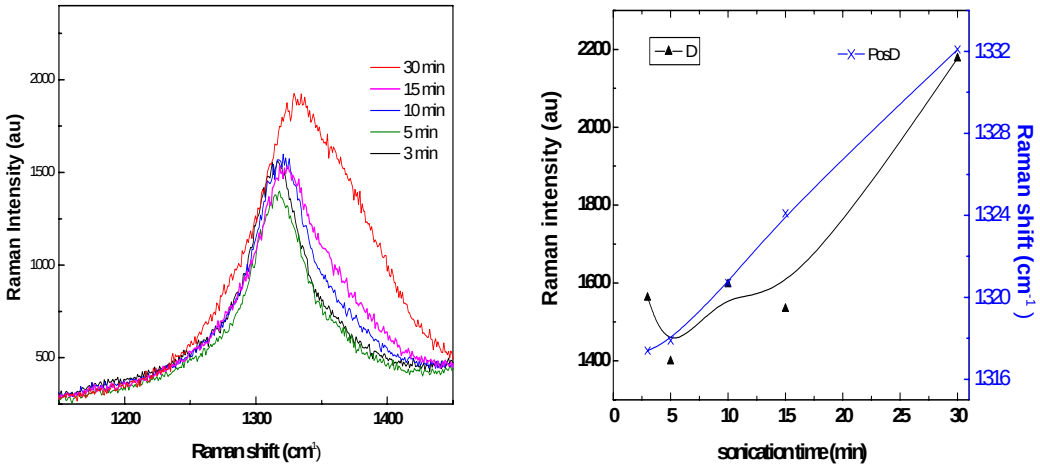

Figure 4.18. (a), D-mode Raman spectrum of SWNTs treated with HNO_3; (b), Raman intensity and shift.

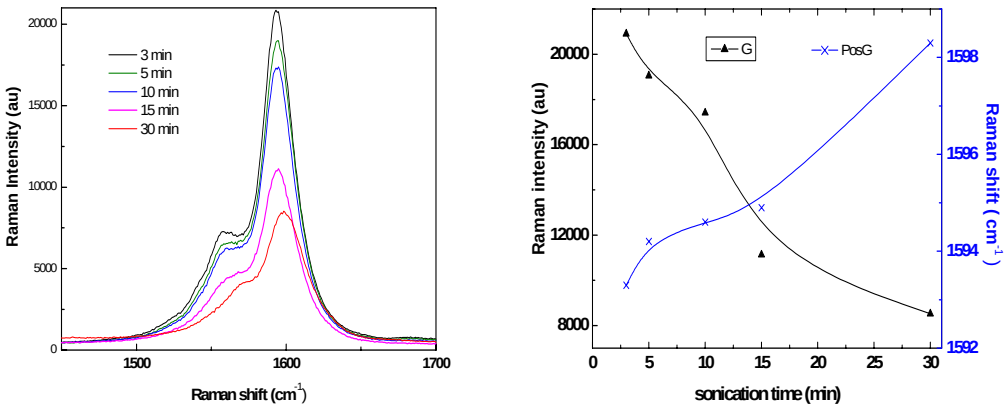

Figure 4.19. (a), As measured G mode of SWNTs treated with HNO_3; and (b), Raman intensity and shift of G mode.

After 10 min laser heating, the G peak increased strongly, with a downshift and narrowed D peak. Further heating diminishes the D and G peak. The SDS sample behaves differently, D and G mode increase after heating, probably because of the smaller magnitude of pertubation.

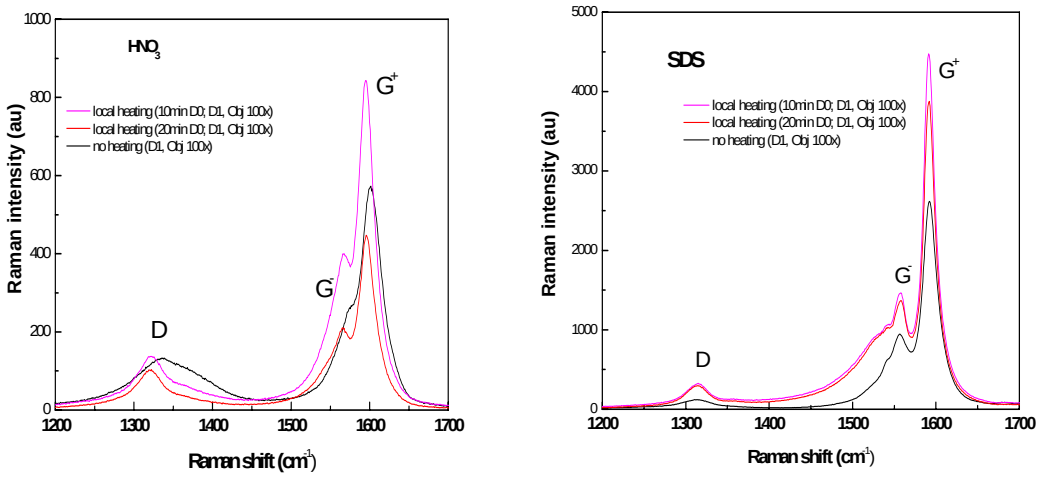

Figure 4.20. D and TM mode of SWNTs sonicated in: (a), HNO_3; and (b), SDS

The shoulder peaks (G^-) of the G mode (G^+) are more distinctive (especially that of the pristine sample), the D peak less intensive. The intensity of the SDS treated samples is more than five times higher than those treated with HNO_3.

The ratio between the intensities of the D- and G-mode is increasing with prolonged sonication, as demonstrated in Figure 4.21. The results indicate that (sp^3-) defects are introduced upon HNO_3 treatment to the SWNT material and the quantity of these defects can be controlled by sonication time.

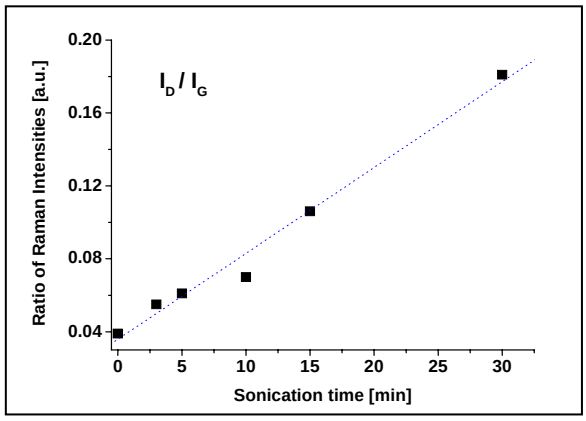

Figure 4.21. Ratio of Raman intensities between D- and G-mode after US/HNO_3 of 3-30 minutes (normalized to the D* Mode).

The increasing D-mode in the Raman spectra could also be explained by functionalization of carbonaceous impurities or by an accumulation of amorphous carbon upon sonication in HNO_3 [135]. Both possibilities are reasonable considering the harsh treatment. The oxygen defect concentration for SWNTs introduced by sonication in HNO_3 was monitored by the shift of the D* line, displayed in Figure 4.22. The line shifts to higher wavenumbers with increasing doping level [136]. The amount of defects increases exponentially after a defect concentration higher than 4%.

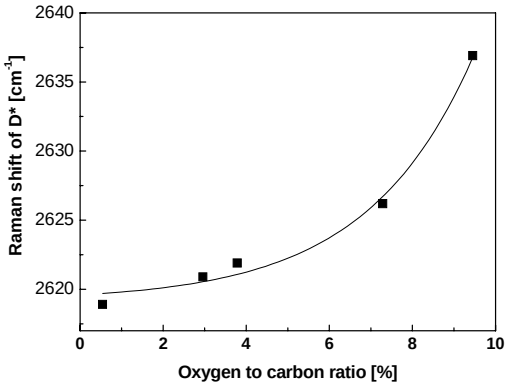

Figure 4.22. Dependence of Raman shift on the oxidation level for D* modes.

Heating of the samples in argon atmosphere leads to a downshift of the G and D* peaks and an increase of the line width at half maximum.The effect can be explained by the removal of oxygen dopants and the subsequent lowering of the hole carrier concentration.

4.4.3 Infrared

Infrared (IR) spectroscopy detects surface-bonded species. A typical infrared spectrum consists of bands, assignable to particular moieties (C=O, C=C, C-OH, etc.) [110]. Carbon monoxide (CO) is the most common adsorbate on the surface of electrodes and finely dispersed catalysts [137]. The band form gives hints on the carbonyl-species, molecular cluster carbonyls have relative sharp bands.

Since HNO_3 is an oxidizing reagent, mainly oxygen containing functionalities are introduced, such as hydroxyl (C-OH), carbonyl (C=O), and carboxyl (COOH) groups (Figure 4.23).

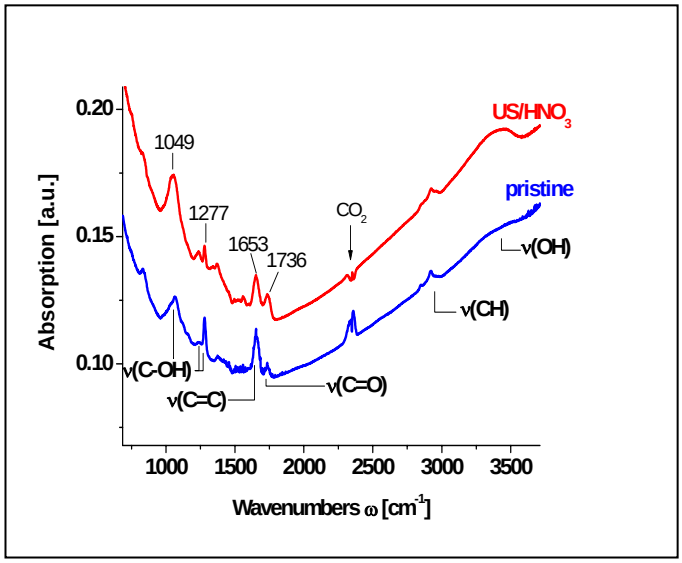

Figure 4.23. IR spectra of SWNT networks US treated in SDS and HNO_3 (3 min).

The upper curve shows the IR spectra of SWNTs sonicated in HNO_3, the lower curve SWNTs sonicated in 1% SDS solution. The SWNT/SDS network already has some functional groups due to the use of ultrasound when preparing the suspension [138]. However, when the SWNTs were sonicated in concentrated HNO_3 the ratio between the intensities of the $\nu_{C=O}$ and $\nu_{C=C}$ oscillations (at 1653 and 1736 cm^{-1}, respectively) is

clearly increasing, which indicates the breaking of C=C bonds and the formation of C=O bonds. Also, a marked increase for the absorption at certain frequencies between 1049 cm^{-1} and 1277 cm^{-1} can be observed, due to the formation of various C-OH functionalities. This leads to the conclusion that mainly hydroxyl, carbonyl, and carboxyl groups are created upon sonication in HNO_3. Spectral features according to NO_3^- ions [272] have not been observed, which suggests that intercalation of HNO_3 is not important. The types of functional groups are in good agreement with previous experiments using a similar sonochemical approach [139],140].

In general, the increasing intensity of the IR absorption at certain frequencies indicates that more functional groups have been created. This can be attributed to an increasing intensity of the Raman D-mode due the creation of oxygen containing functional groups upon US/HNO_3 treatment.

4.4.4 UV/Vis/NIR

It is reasonable to assume that US/HNO_3 treatment introduces p-type doping of SWNTs. Oxygen is known to be an electron acceptor due to its higher electronegativity compared to carbon. Even oxygen physisorbed on the surface of CNTs has been reported to be a p-dopant [141,142]. Since the addition of oxygen containing groups increased the conductivity, it is possible that covalently bound functional groups containing oxygen also act as p-dopants. This assumption has been confirmed by UV/Vis/NIR spectra (Figure 4.24) for energies from 0.5 to 2.5 eV.

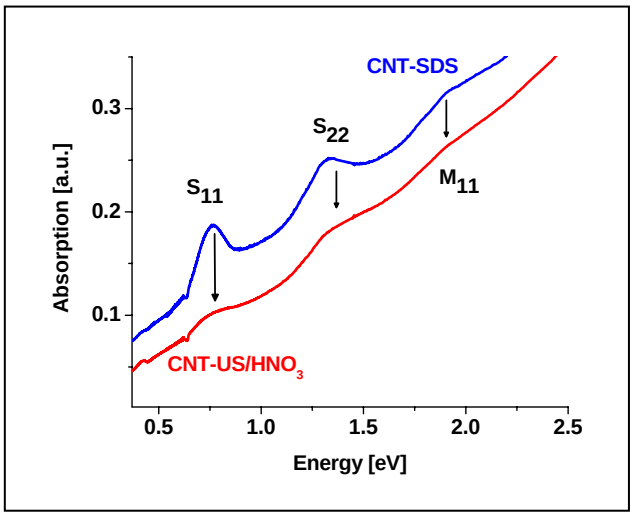

Figure 4.24. UV/Vis/NIR spectra of SWCNT networks before and after sonication in concentrated HNO_3 for 3 min.

The dominating features in the spectrum of the reference sample (sonicated in SDS instead of HNO_3) are three peaks between 0.7 eV and 2.1 eV. They can be attributed to electronic transitions between the van Hove singularities of semiconducting (S_{11} and S_{22}) and metallic (M_{11}) CNTs [120]. After US/HNO_3 treatment for 3 minutes, a clear decrease can be observed indicating a loss of electrons [72,120].

4.5 Brunauer-Emmett-Teller method

The total surface area of SWNT networks can be determined using the *Brunauer-Emmett-Teller (BET)* method based on nitrogen adsorption isotherms. Luo et al. [49] report a BET surface of 180 m^2/g for SWNTs prepared by CO disproportionation followed by HNO_3 treatment and air oxidation. Measurements by Du et al. [52] on purified HiPco samples exhibit surface areas of 861 m^2/g. Specific surface values for HiPco and other SWNTs of 1600 m^2/g are reported after complete purification [129]. In this work the specific surface areas did not exceed 800 m^2/g with a maximum value for the HNO_3-treated samples. The nitrogen BET surface area of a BP was measured between ~700 to 800 m^2/g, depending on treatment. Oxidizing purification procedures

are reported to increase the total surface area and micropore volume of the HiPco material possibly due to tube opening [143].

Table 4.5. BET area values of various SWNTs [144].

Treatment	*A* (m^2/g)
Powder (raw)	738
Powder (oxidized, air)	696
Bucky paper (oxidized, HNO_3)	797

Monte Carlo molecular simulations predict BET values as high as 3000 m^2/g for open SWNTs of 3 nm diameter with a 0.4 nm spacing between adjacent tubes (compared to commercially available activated carbons ~1000 m^2/g [145]).

4.6 **Scanning electron microscopy**

Scanning electron microscopy (SEM) is useful for high-resolution recording of electrode surfaces. The top view of the SWNT electrode indicates the rough surface of the gas diffusion layer (Figure 4.25a) and the even catalyst layer (Figure 4.25b). The related cross sectional SEM image in Figure 4.25b clearly shows the double-layered structure with the hydrophobic (A) and hydrophilic (B) part of the electrode.

The cross-sectional view of Figure 4.26 shows the porous structure of the GDL (A) with the attached homogeneous CL (B). It is a proof of the compact SWNT electrode architecture and with a very low thickness of ~10 μm. In analogy to commercial gas diffusion electrodes the hydrophobic property of the SWNT electrode is realized by admixing PTFE to the SWNT network. Figure 4.25.a. shows the network structure of the GDL with PTFE in high concentration. It shows an enlarged part of the

hydrophobic PTFE functionalized side after annealing. The PTFE appear as individual particles distributed along the SWNTs rather than a separate layer.

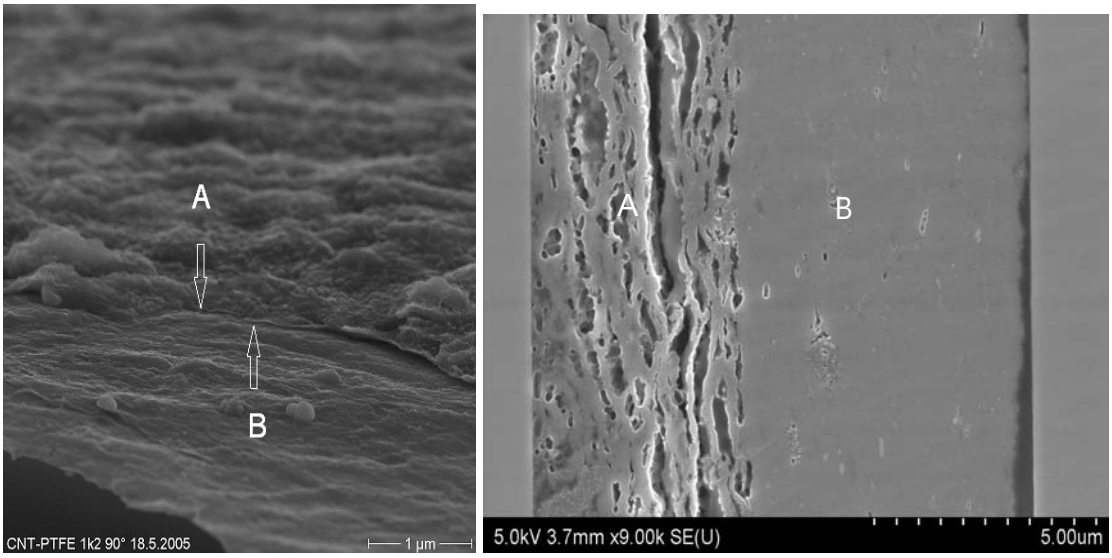

Figure 4.25. (a), Top view of SWNT electrode; and (b), cross section with GDL (A) and CL (B).

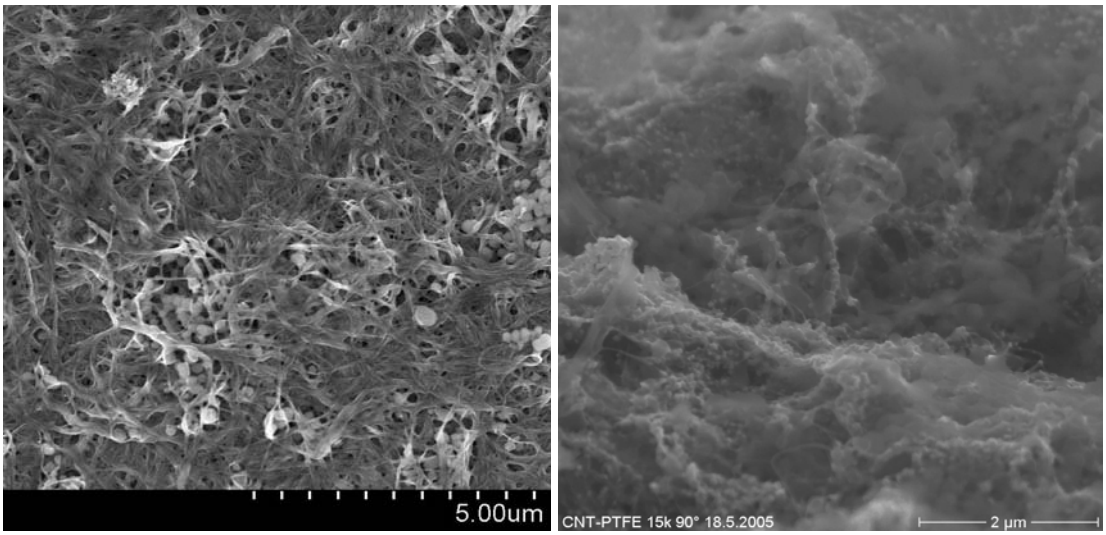

Figure 4.26. (a), GDL structure; and (b), magnification.

The catalyst layer (Figure 4.27.a) also shows clear porosity. Partially, the SWNTs are organized in form of bundles of several hundred nanometers (Figure 4.27.b).

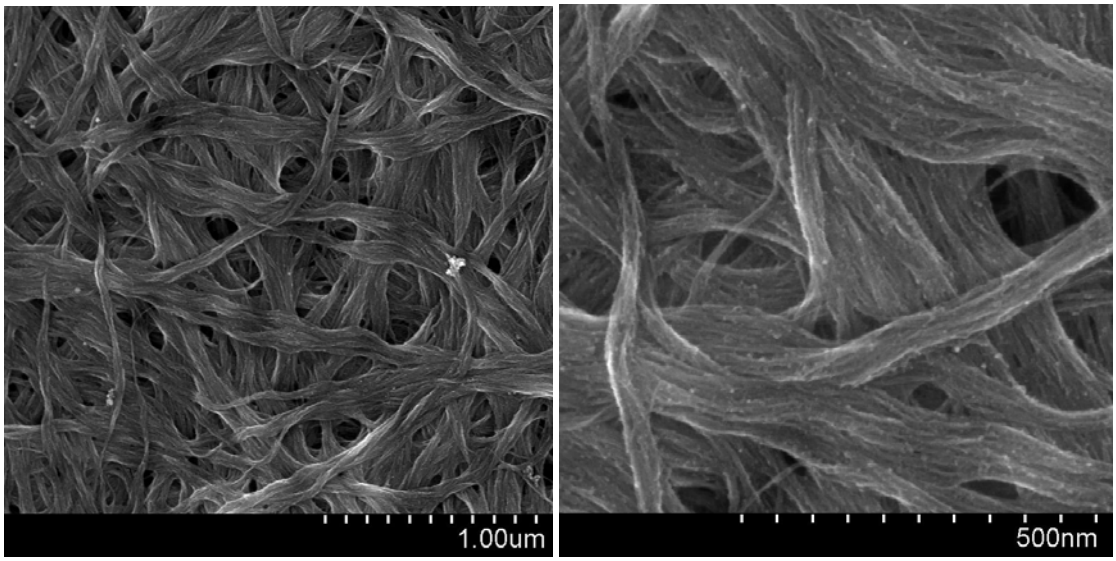

Figure 4.27. (a), CL structure; and (b), magnification.

4.7 **Transmission electron microscopy**

The size of catalyst particles is typically recorded by *transmission electron microscopy* (TEM) images [11]. For comparison with commercial E-TEK electrodes (Figure 4.28.a) the platinization procedure described in [81] was also applied to catalyst-free Vulcan XC-72, so called 'backings' (Figure 4.28.b) and for SWNTs (Figure 4.28.c).

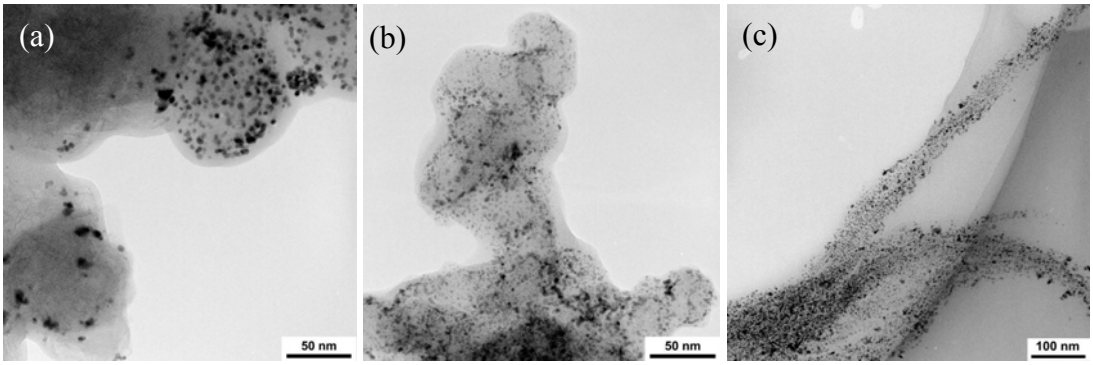

Figure 4.28. (a), Commercial catalyst layer (E-TEK); (b), platinized Vulcan XC-72; and (c), platinized SWNT bundles.

As shown in Figure 4.29 the catalyst (dark spots) is distributed homogeneously in the SWNT network. For statistical evaluation different sample regions (red circles Figure 4.29.a) were chosen to determine catalyst size and distribution (Figure 4.29.b). Figure 4.29.c displays the structure of the catalyst layer comprising open tube ends (x), aligned tubes (y) and Pt particles (z).

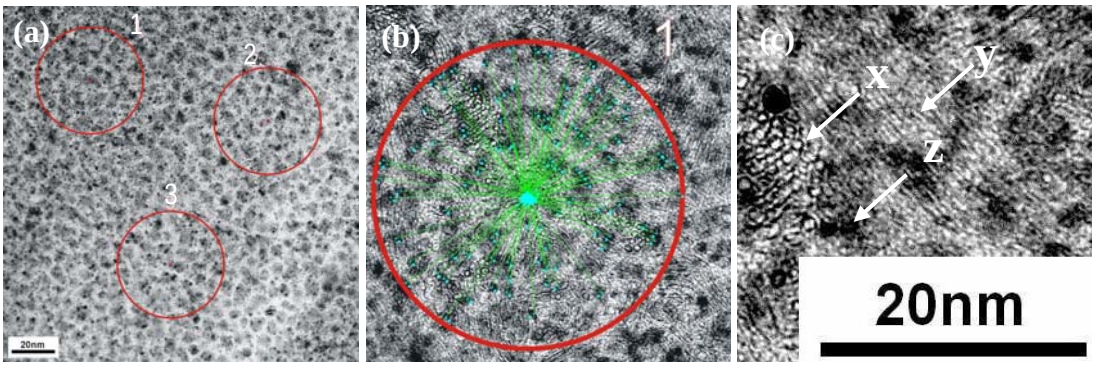

Figure 4.29. TEM images of catalyst layer: (a), statistical evaluation; (b), size/distance identification; and (c), enlarged structure details.

The Pt particles with an average size of 1.4 nm (Figure 4.30) are appropriate for the catalytic reactions at anode and cathode although their size is smaller than the optimum size of 3 to 4 nm [91]. The observed increase of the Pt amount with spherical

extension indicates homogeneous catalyst distribution (Figure 4.30.b). The quadratic growth fit in Figure 4.30.a is drawn as a guideline for the eye.

The density of the catalyst particles and their homogeneous distribution is analysed by the interparticle distance distribution. Since the number of particles scale with the sphere around a chosen center point, the occurrence (frequency) of catalyst particles will be ~ x^2 (with x the distance from center to neighbouring particle). The solid line in Figure 4.30.b indicates that such a behaviour is followed, i.e. the catalyst particles are distributed homogeneously in the investigated electrode part.

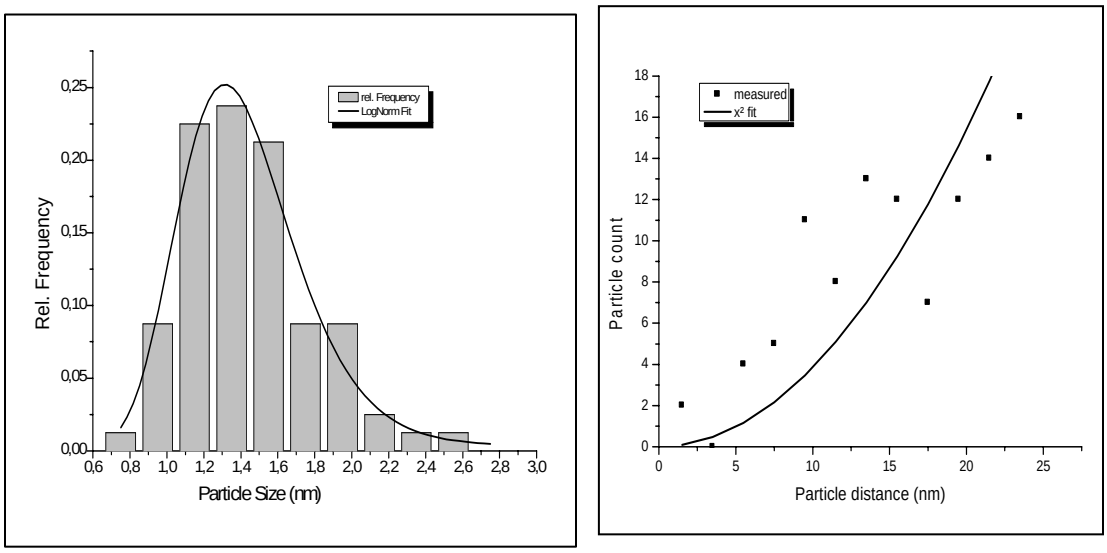

Figure 4.30. (a), Catalyst size distribution with log normal fit (solid line); and (b), catalyst density/ homogeneity.

The layered structure of the GDE in Figure 4.31.a was originally disrupted (large white areas) causing a distortion of the GDL thickness. The dense hydrophilic catalyst layer ('SWNT', dark grey) adjoins the hydrophobic GDL ('Teflon layer'). Figure 4.31.b shows the interpenetrating network of nanosized SWNT bundles ('SWNT') and micro-

sized PTFE ('Teflon'). The white arrows indicate the interfaces between the hydrophobic and hydrophilic components.

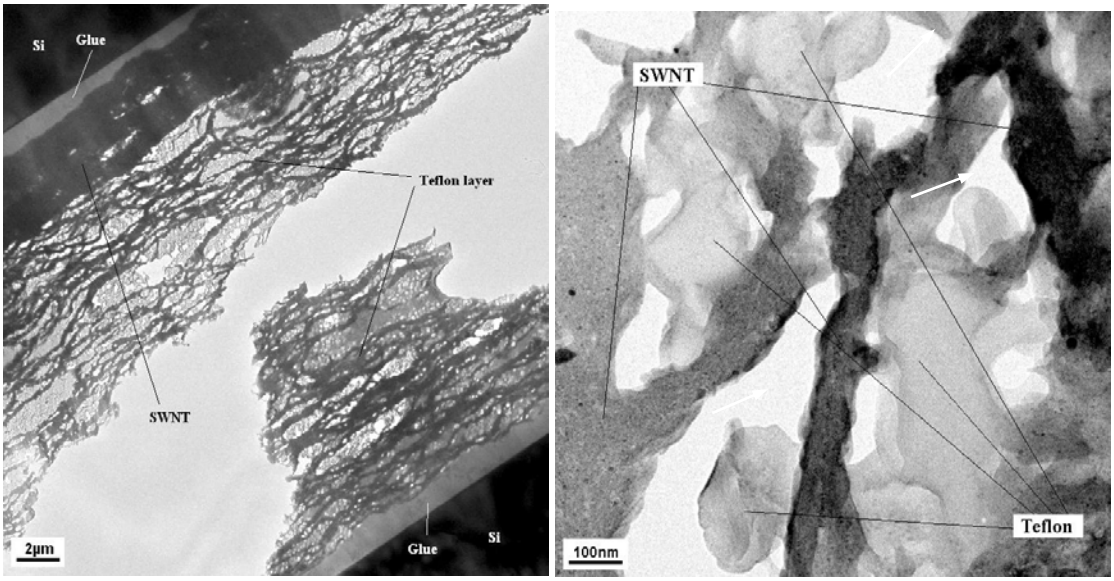

Figure 4.31. (a), Cross section of GDE; and (b), magnification.

4.8 **Fuel cell testing**

4.8.1 Membrane electrode assembly

For fuel cell testing, the SWNT electrodes (Figure 4.32.a) were placed in a home-built fuel cell array (Figure 4.32.b) consisting of endplates with meander, gas in- and outlet and flow fields for gas distribution. The SWNT gas diffusion electrodes were placed with the hydrophobic side facing the flow fields. The hydrophilic side is attached to a filter membrane (Figure 4.32.c) acting as a gas separator/electrolyte. The filter membranes were thoroughly wetted with conc. H_3PO_4 to achieve high proton conductivity before the fuel cell was sandwiched together.

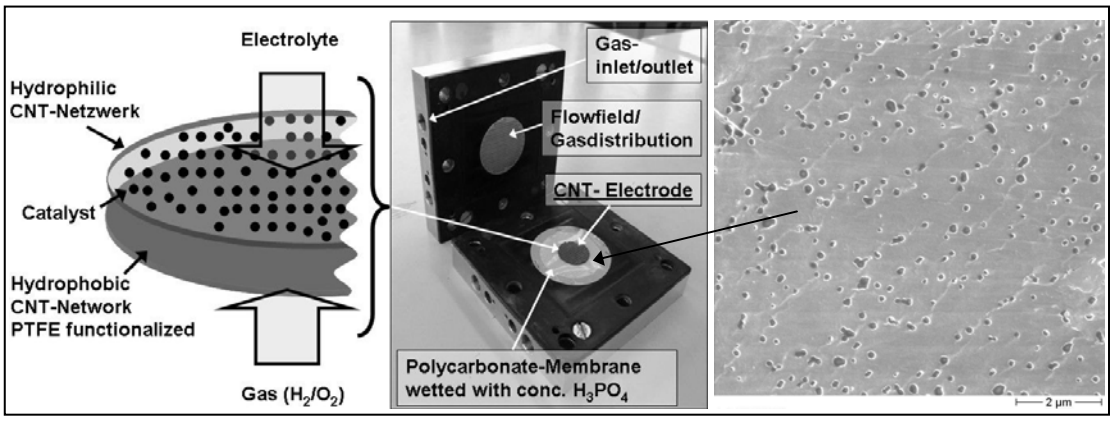

Figure 4.32. (a), Sketch of the SWNT GDE; (b), fuel cell setup; and (c), SEM image of PC membrane.

PC/H_3PO_4 membranes are a flexible separator providing a simple and anhydrous electrolyte without the need for humidification. The used ion-track membranes [18] are 6 µm thick with pore diameters of 10 nm and densities of 6 $x10^8$ pores/cm^2 [107]. Practical considerations of membrane strength require a minimum membrane thickness of 5 µm thick [146]. The chemical stability of PC membranes with concentrated H_3PO_4, is limited to temperatures <140°C [147].

The pores of the filter membrane are sufficiently small to retain the electrolyte at pressure differences of > 6 $x10^3$ Pa. For comparison, membranes like Nafion® N-117 [148] have a thickness of 175 to µm requiring complex humidification. A comparison of the relevant membrane/electrolyte properties of PC/H_3PO_4, PC as filter membrane and Nafion are given in Table 4.6. PC/H_3PO_4 proved to be simple, thin, light weight and inexpensive alternatives to the stiff and much thicker PAFC matrices made usually of SiC.

Table 4.6. Electrolyte/membrane properties [103,107,148].

	PC/H_3PO_4	*PC*[b]	*N-117*
Pore size (nm)	10	100	
Nominal thickness (μm)	6	6	175
Pore density (pores/cm^2)	6 x 10^8	4 x 10^8	
Weight caliper (mg/cm^2)	0.7	0.7	36
Max. operation temp. (C°)	150	150	100
Water flow rate[a] (ml min^{-1} cm^{-2})	< 0.1	2	
Water content (%)	<1%		38[c]
Protonic Conductivity $\kappa_{300\ K}$ (S/cm)	0.05		0.06
Activation energy $E_{a\ 300\ K}$ (eV)	0.3		0.22

[a] 25°C, 10 psi (0.7 $kgcm^{-2}$) [b] used for filtration
[c] soaked at 100°C for 1h (dry weight basis)

Commercial electrodes (Vulcan XC-72) were used throughout as reference electrodes. The effective electrode surface was constantly 3 cm^2 with 20% Pt/C Pt/SWNT electrodes with a Pt loading of 0.4 mg/cm^2. Pure H_2 and O_2 gases (5.0, i.e. 99.999% purity) were used without any humidification with a-C electrode either on the cathode or the anode side.

4.8.2 Current and power density curves

With a power density of 425 mW/cm^2 at 175°C the catalyst preparation and fuel cell setup proved to be compatible to conventional PAFC setups. I/V curves were taken at several temperatures ranging from room temperature to 125°C (Figure 4.33). The influence of the operation temperature is obvious, showing decreasing and ohmic losses with increasing temperatures.

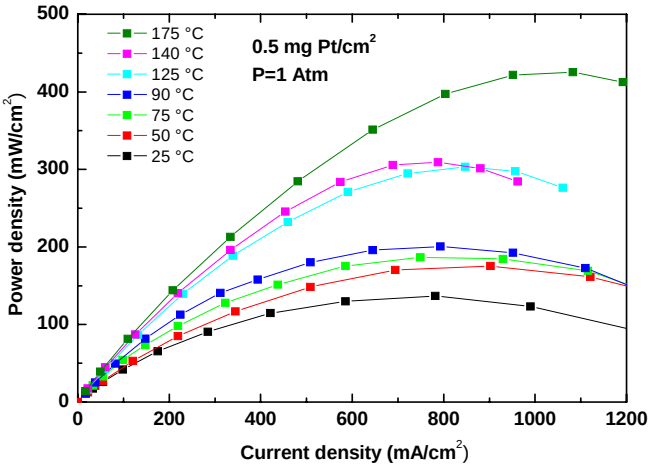

Figure 4.33. Performance of platinized catalyst-free Vulcan XC-72.

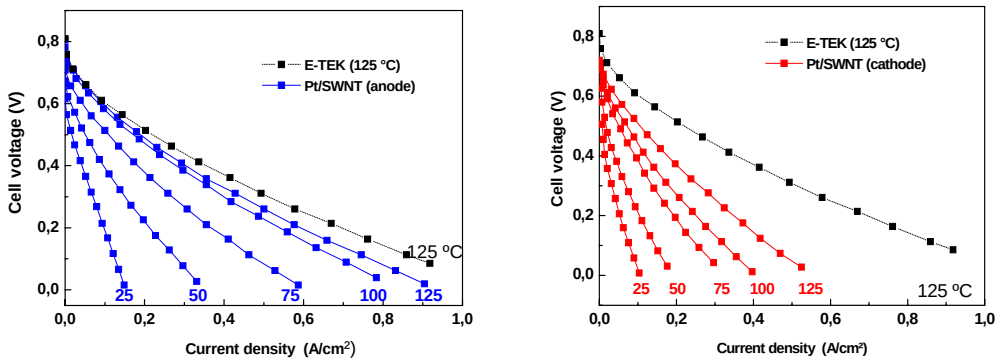

Figure 4.34. Half cell measurements of SWNT and E-TEK electrodes: (a), anode; (b), cathode between 25 and 125 °C.

At the same temperature, the performance of the anode (H_2 side) is comparable to commercial a-C electrodes (for clarity, shown only for 125 °C). The performance of the cathode (O_2 side), however, is appreciably lower and only 2/3 of the E-TEK performance is achieved. This can be attributed to non-optimized wetting characteristics of the cathode as emphasized by Bett et al. [149]. Furthermore, the catalyst size is not optimized (1.4 nm instead of 3 nm).

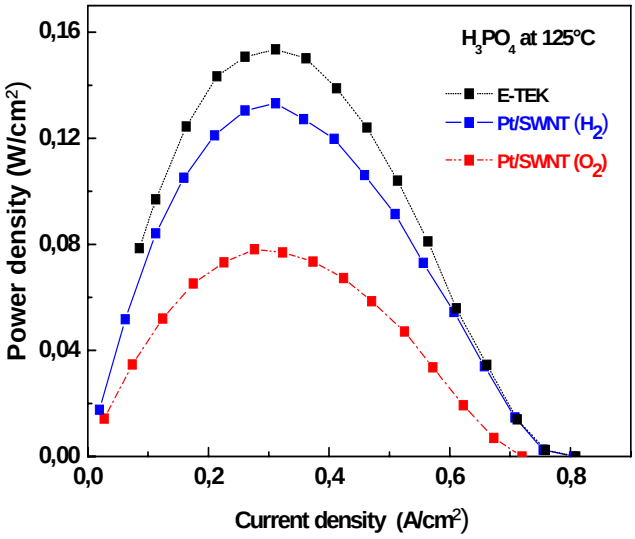

Figure 4.35. Performance curves E-TEK and SWNT electrodes.

The performance curves strongly depend on the preparation parameters, especially sonication. Increasing sonication during sample preparation leads to higher power densities, illustrated in Figure 4.36. This can be attributed to the higher Pt load shown by EDX data (Table 4.3).

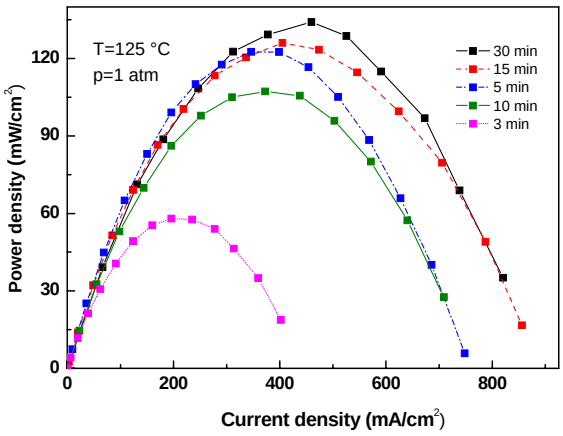

Figure 4.36. Sonication time and performance (SWNT anode).

SWNT electrodes were tested after SDS treatment showing peak power densities of up to ~200 mW/cm^2 at 125 °C (Figure 4.37). The SDS treated samples show higher power densities than the samples sonicated in HNO_3.

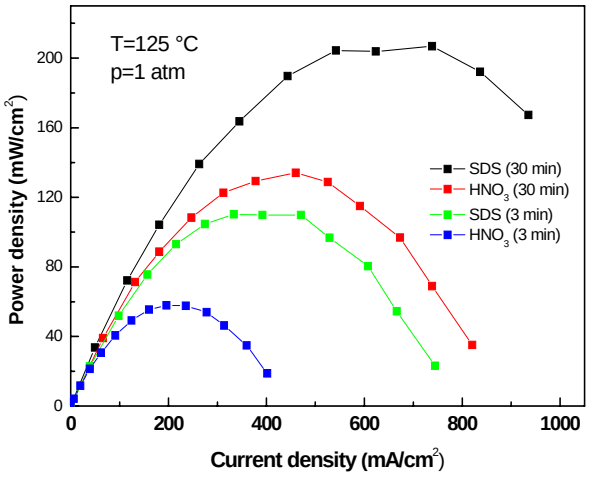

Figure 4.37. Performance of SDS vs. HNO_3 treated samples (SWNT anode).

4.9 **Discussion**

It is shown that freestanding SWNT networks have the potential to fully replace a-C electrodes. The processing from liquid suspensions allows flexible electrode designs and open new ways for significantly mass-/volume-reduced H_2/O_2 fuel cell electrodes. The high conductivity of SWNT networks (up to ~2,400 S/cm) compared to a-C (~ 1 S/cm) allows a strong reduction of the electrode thickness (typical 10 µm). Functionalization/doping by US/HNO_3 treatment of SWNTs leads to both increased conductivity and destruction of the molecular structure. The trade-off for a maximum conductivity of SWNT networks (buckypapers) is reached when nearly 2% of all C-atoms are oxidized. IR absorptions due to NO_3^--ions were not observed, so

intercalation of HNO_3 is negligible. Thus the increased conductivity can be explained in terms of doping of the semiconducting SWNTs which are the majority in bulk SWNT samples.

With reduced electrode thickness the catalyst is confined to a narrow zone adjacent to the membrane. The catalyst particles are distributed homogeneously within the SWNT networks. The Pt particles are appropriate for the catalytic anode and cathode reactions, their average diameter however, is clearly under the optimum catalyst size of ~3 nm. Further improvement is expected for: (a), electrode thickness reduction to the nm-scale; and (b), catalyst size adjustment.

For isolated SWNTs and particular SWNT networks the thermal resistance is uncritical. In this context it was shown by Raman spectroscopy that gradual/stepwise heating is a means to expose SWNTs to higher temperatures. Furtheron, SNWTs made by precious catalyst like Rh/Pt/S are more resistant to thermal oxidation. The thermal stability is by far appropriate for fuel cell application, as demonstrated by the fuel cell tests at $100 < T < 150$ °C (PAFC test).

For the fuel cell electrolyte a simple arrangement has been chosen: a polycarbonate filter membrane (pore size 10nm) was soaked with conc. H_3PO_4 establishing the required proton conductivity between the SWNT anode and cathode (SWNT-PAFC). Since conc. H_3PO_4 has been used as electrolyte, I/V curves could have been taken at temperatures up to 150 °C where catalyst poisoning is less critical. The fuel gases did not require humidification. The performance results agree with those of recent HT-PEFCs such as PBI/H_3PO_4 [150,151] and conventional PAFCs [152]. Evidently, the thin film SWNT-PAFC is competitive with the well-established PAFC and HT-PEMFC.

The power densities of the SWNT electrodes and of commercial a-C electrodes (E-TEK) at 125 °C differ only slightly for the anodic half-cell reaction indicating that

none of the carbon materials has a distinct advantage. This suggests that the catalyst-support interaction is quite similar for the different forms of carbon. An increase in temperature (>>125°C) will have a beneficial influence on performance by the reduction of the ohmic loss but was renounced to conserve the home built fuel cell array (sealing, gold plating). The appreciably lower performance of the SWNT cathode compared to the SWNT anode can be explained by the fact that the cathode involves a different activity of the catalyst and a complex 4e- chemical reduction process [74]. Having both a tuned wetting behaviour and highly distributed small diameter catalyst particles, all the requirements for a technically exploitable GDE are fulfilled.

5 The MWNT electrode

Dense and vertical aligned MWNTs are considered as gas diffusion layers [37], catalyst support layers [153] and electrodes [154]. MWNTs are also promising materials for batteries, capacitors and chemical filters [155,146]. The concept of tailored MWNT gas diffusion electrode (GDE), in the following named 'electrode', under special consideration of the inner tube diameter is outlined in this chapter.

5.1. **Concept**

For such MWNT fuel cell electrodes, aligned tubes, often called 'MWNT forests', would comprise the gas diffusion and catalyst layer forming a concrete three-phase zone. Since these MWNT forests are mechanically unstable they have to be fixed, e.g. within a polymer matrix. The MWNT tube length and pore diameter (Figure 5.1) can be used to define the thickness of the GDE (δ) and channel size for direct gas supply. For such a device the catalyst layer would be at one of the tube ends (b) overlapping the stabilizing polymer (c) in contact with the electrolyte (d).

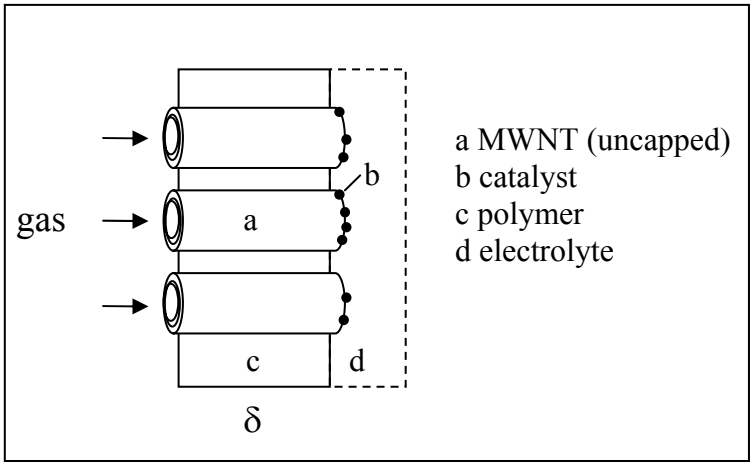

Figure 5.1. Aligned MWNT electrode (schematic)

Vertically oriented MWNTs can function as the gas distribution network supplying the catalyst layer [156] with the fuel gas. Furthermore, they can improve gas diffusivity and electronic conductivity [157]. To establish a three-phase contact between electrolyte and current collector the tube ends have to be opened.

Elements and compounds that wet graphite (surface tensions of < 190 mN/m) potentially can fill nanotubes [158]. Water with a surface tension of ~73 mN/m [159] can fill nanotubes [160]. The size constraint on capillary filling of nanotubes can be exploited to avoid flooding of the tubes with the electrolyte. For MWNTs with diameters of 1 to 2 nm filling with liquids is not possible [158]. Fast flow velocities are reported from the frictionless nature of the CNT walls [161,162], especially when using gases (e.g. oxygen ~13 mN/m [163]) instead of liquids.

The type of growth catalyst material, thickness and growth conditions (temperature, gas pressure) have an influence on purity, diameter, alignment and quality of the CNTs [164]. The nanotube size is set by the diameter of the catalyst particle used for its growth [165,166]. The inner diameter distribution of MWNTs (1.5 to 2 nm) is close to those of SWNTs (1 to 2 nm) [22,23]. Innermost tube diameters of less than 1 nm are reported for the arc discharge method using hydrogen gas [167]. For comparison, nanotube outer diameters range between 30 nm [168] and 100 nm with a larger variation in height (length) of taller nanotubes (10-15 μm) [169].

The nanotube length depends on the deposition time. Corresponding growth rates range from 20 μm/min (CVD) [170] to 330 nm/min (plasma enhanced chemical vapor deposition, PECVD) [169]. The density of MWNTs can be controlled by the thickness of the underlayer and growth catalyst layer [153]. The degree of alignment parallel to each other depends on the number of CNTs per unit area of the substrate [170]. Reducing the nanotube inter-distances (100–250 nm [171]) enhances parallel growth. The attachment of Pt particles, mainly located at the MWNT tips [172] require an oxidative opening of the tube ends on the catalyst side. The catalyst particles within the three-

phase zone are located in a well-defined area at the MWNT ends. Tube diameter and the degree of functionlization determine the catalyst load.

To summarize: the steps to form an aligned MWNT-electrode comprise the synthesis of vertically aligned MWNT forests, the fixation of the MWNT structure, opening of tubes and catalyst deposition.

5.2. **Sample preparation**

MWNTs were directly grown on silicon (Si) /silicon oxide (SiO_2) substrates using the CVD technique. For MWNT growth the SiO_2 substrates were coated with iron catalyst and exposed to acetylene and ammonia. Acetylene was used for the carbon source, ammonia for reduction of the metal catalyst. The aligned MWNT arrays were grown in the hot zone of the furnace between 700 to 800°C, in accordance with [42]. Carbon tubes can also be synthesized by CVD within the pores of commercially available alumina template membranes [155]. Those carbon nanotubes have the same outer diameter as that of the pores of the template membrane, they are uniform and hollow with open ends [173].

The fixation procedure is a necessary step to ensure that the aligned MWNTs remain mechanically stable. Besides coating the aligned MWNTs with polystyrene (PS) [146,174], parylene-N/MWNT films were prepared by vapor deposition of parylene-N. Parylene-N (poly(*p*-xylylene)), is a highly crystalline, polymer produced by vapor-phase deposition and polymerization of para-xylylene [175] with a melting temperature of 410 °C [166].

5.3. **Results**

MWNTs grown on a silicon wafer form a well-aligned CNT forest seen in Figure 5.2.a. The characteristic Raman peaks of the MWNT samples are shown in Figure 5.2.b. As usual for MWNTs the RBM signal is not detectable. The values for the relevant D, G, D' modes can taken from Figure 5.2.b.

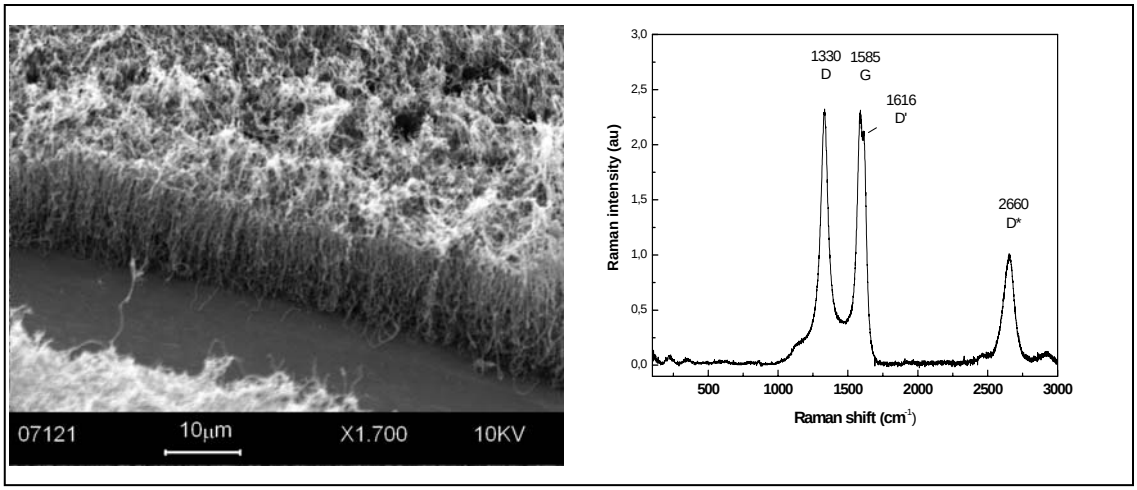

Figure 5.2. (a), As-grown MWNTs on silicon wafer; and (b), normalized Raman modes of pristine MWNTs.

Unlike dip or spray coating, parylene coating proved to be uniform and was thus applied. However, in the pristine and oxidized state the polymer does not wet the MWNT forest (Figure 5.3.a and Figure 5.3.b).

The wetting properties of the MWNTs were adjusted. Therefore the aligned MWNT mats were oxidized at 600°C for 10 min and subsequently reduced with hydrogen at 700°C for one hour. The surface groups like C=O and COOH, introduced during the

oxidation are most likely reduced C-H functionalities. The nonpolar C-H groups (sp^3-bonds) are necessary to impregnate the MWNT structure with parylene. The effect of

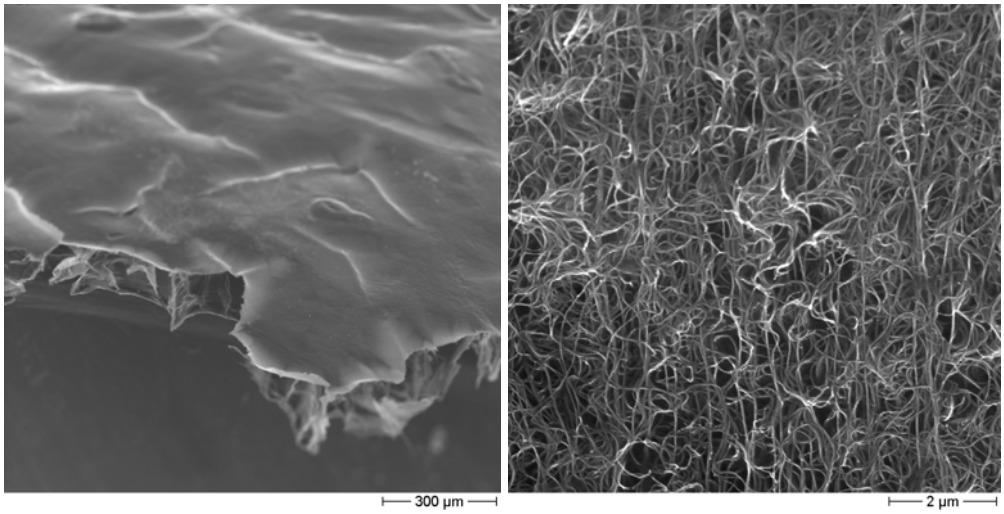

Figure 5.3. Non wetted MWNT forests: (a), top; and (b). side view.

surface modification based on oxidation and subsequent reduction is visualized in Figure 5.3. The D mode (Figure 5.4.a) increases with increasing oxidation time due to the higher oxygen defect density without a Raman shift. A weak Raman downshift (from 1330 to 1325 cm^{-1}) of the D mode in Figure 5.4.b can be observed after reducing the MWNT samples in hydrogen.

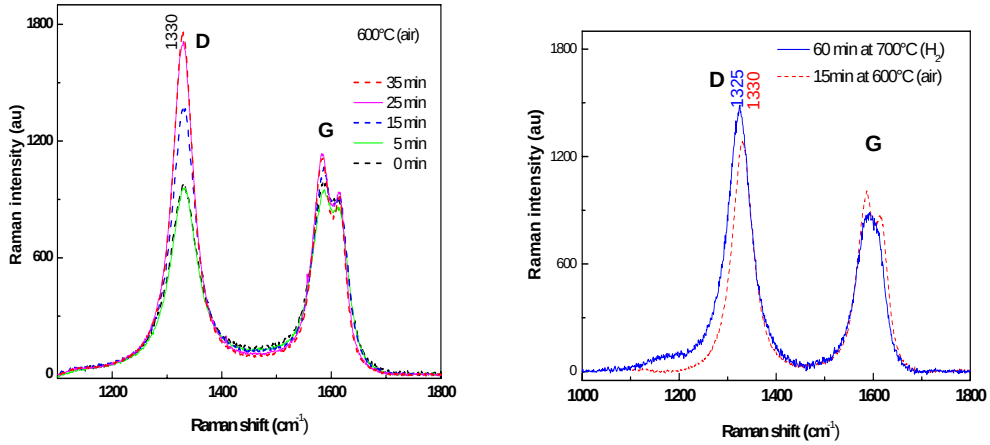

Figure 5.4. Raman spectra of: (a), oxidized; and (b), reduced MWNTs grown by CVD.

Hydrogen treatment minimizes the charge density by the removal of p-dopants. The extent of a Raman up-/down shift can therefore be used as an indicator for the level of doping. The full width at half maximum (FWHM) of the D mode increases after heat treatment with hydrogen Similar results for the D* mode reported for samples heated in argon [136].

Complete coating was realized showing a well aligned and fixed MWNT structure after polymer imbedding in Fig. 5.5.a-d. The 'bubbly' composite surface (Figure 5.5.a) can be explained with length differences of the as grown MWNTs. Interestingly, the impregnation with parylene is stronger on the SiO_2-faced side (Figure 5.5.b, bottom). The highly anisotropic character of the deposited parylene-N with layered chains can be seen in Figures 5.5.c and Figure 5.5.d confirmed in [175].

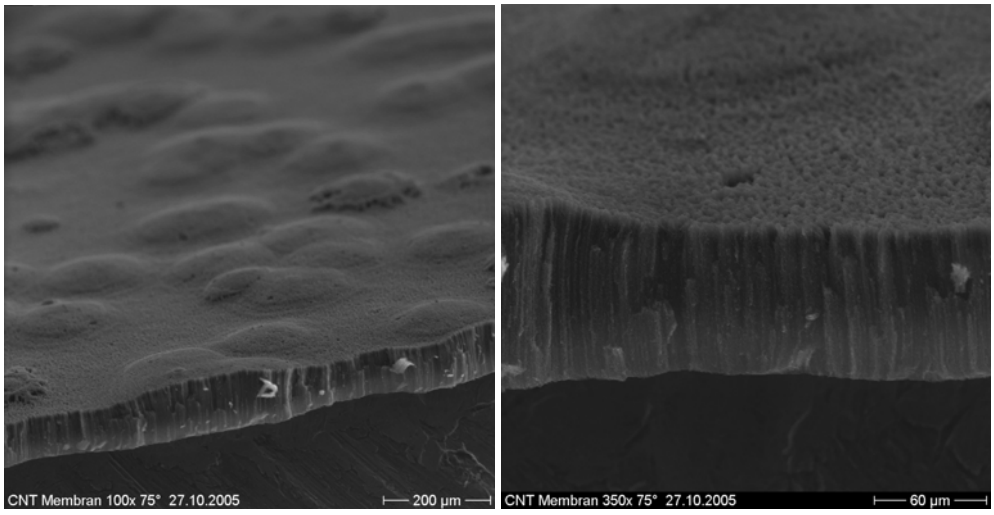

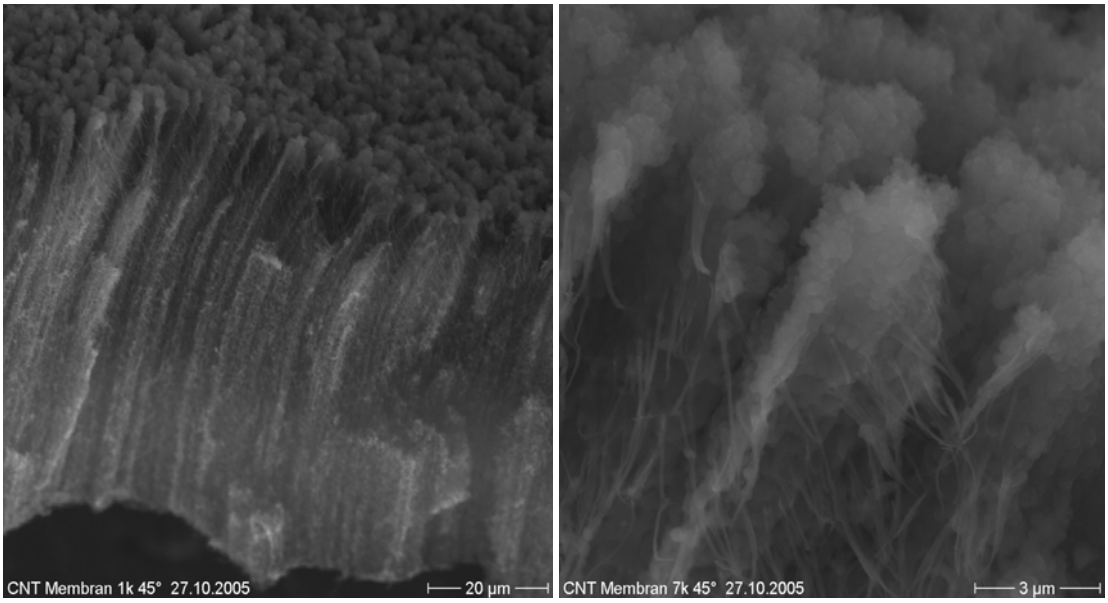

Figure 5.5.a-d. MWNT/parylene composites of reduced MWNT (various magnifications).

The MWNT/parylene film was removed from the silicon substrate by etching in a 30wt% KOH solution at 80-100°C. Instead of HF solution as proposed by [146], KOH proved to be a convenient and less aggressive etchant. After a few minutes the composite film separated from the substrate through dissolution of Si and SiO_2 layer leaving a flexible and stable film. The films are highly electric insulating due to the coating with parylene. Plasma oxidation was then performed to remove the excess of polymer. Reactive ion etching of parylene-N in oxygen plasma has been demonstrated by Tactito et al. [176] initiated by oxygen atom-induced or hydroxyl radical-induced hydrogen abstraction reactions [246].

5.4.**Discussion**

Alternatively, the electrode structure using fully aligned MWNTs presents a kind of model system. Notably the dimensions (thickness and lateral extension) can be

controlled by the deposition process of the growth catalyst (structure) and the growth parameters (CNT length or electrode thickness, respectively). The rather fragile aligned MWNT structure can be stabilized by imbedding it in a polymer matrix. (vapour deposition of Parylene N). Subsequent plasma etching of excess polymer material can be used to uncover the tips of the MWNTs.

The described approach allows tailor electrodes with respect to thickness and pore size. Downsizing the electrode thickness towards the nm-scale increases the demand for defect-free GDEs. This requires an accurate control of homogeneous tube size, homogeneous coating and etching to assure mechanical integrity and reproducibility. CVD of nanocarbon materials still requires relatively high deposition temperatures. Plasma enhanced vapor deposition (PECVD) [41,169] can offer lowered deposition temperatures, however with shortcomings like reduced growth rate and length [177]. For comparison: at ~700 °C well-aligned tubes form, uniform in size, whereas at higher temperatures (~900 °C) nanotubes become disordered and less aligned [41].

Catalyst deposition on MWNT tips has already been demonstrated in [153] and should not be the crucial part. A lack of transversal current because of dielectric fillers is of minor importance since the chosen design electron flow along the tubes fulfils this function. Future work would require the optimization of the growth/etch parameters, as for example shown in [178].

Filling of nanotubes (at moderate temperature and pressure) is a relative new field of investigation requiring further insights for reliable size exclusions. Especially at elevated temperatures this aspect becomes more crucial. Specific functionalizations like fluorination of the MWNT tips could improve the wetting behaviour. Gas permeability/diffusion test should be carried out in parallel to monitor possible mass transport limitations.

6 Conclusions and Outlook

The work presents the characterization of novel fuel cell electrodes based on SWNTs and platinum as the main constituents. The suitability of such SWNT electrodes as an alternative for conventional fuel cell electrodes based on a-C has been confirmed by different spectroscopic and electrical measurements. Additionally, a new approach by aligned MWNTs has been demonstrated which allows topologically more ordered/defined arrangements of catalyst layer and gas diffusion layer. The more ordered electrodes based on vertically aligned MWNTs are expected to further improve fuel cell performance which has to be verified by forthcoming experiments, however.

In comparison to conventional electrodes, the new SWNT electrodes make use of only one carbon material and liquid state processing, thereby simplifying preparation. The advantages of PEFCs with thin flexible electrodes, high current density and low weight, were combined with the enhanced operating temperatures of PAFCs. Together with an unconventional electrolyte solution this enables a significantly mass- and volume-reduced fuel cell. The SWNT-PAFC fuel cell shows performance levels comparable to cells with long-term optimized commercial electrodes. The SWNT electrodes are in the proof-of-concept status and further improvements should focus on the partial hydrophobization of the catalyst layer to reduce mass transport limitation by electrode flooding as well as on optimum size catalyst particle preparation.

Further progress will require the elimination of defects and other reaction products/impurities in CNTs , production in high yield (to lower the actual high price of CNTs with 500$/g 179 to decrease costs), and synthetic control of tube properties (diameter, length, chirality, number of concentric layers). Using a mass-oriented performance definition of fuel cells, e.g. W/g as proposed by Gottesfeld and Zawodzinski [77] would underline the advantages of SWNT as electrode material.

Increased de-bundling of the SWNTs will help to enlarge the specific surface area, further reduce the electrode thickness and increase porosity. The high achieved conductivity values are not mandatory and may be sacrificed to longer tube length by using e.g. moderate sonication (e.g. US/SDS). Future work should emphasize on long-term stability and optimization of the cathode.

Bibliography

1 M.S. Dresselhaus, *Nature*, 358, 195 (1992)

2 A. Jorio, R. Saito, G. Dresselhaus, M.S. Dresselhaus, *The Royal Society*, Phil. Trans. R. Soc. Lond. A, 362, 2311 (2004)

3 R. Saito, G. Dresselhaus, M.S. Dresselhaus, *Physical Properties of Carbon Nanotubes*, Imperial College Press London (1998)

4 W. Justi, W. Winsel, *Kalte Verbrennung- Fuel Cells*, Franz Steiner Verlag (1962)

5 K. Kordesch, G. Simader, *Fuel Cells and Their Applications*, Wiley-VCH (1996)

6 L.J. Blomen, M.N. Mogerwa, *Fuel Cell Systems*, Plenum Press (1994)

7 M.S. Dresselhaus, G. Dresselhaus, K. Sugihara, I.L. Spain, H.A. Goldberg, *Graphite Fibers and Filaments*, Springer-Verlag (1988)

8 H.W. Kroto, J.R. Heath, S.C. O'Brien, R.F. Curl, R.E. Smalley, *Nature*, 318, 162 (1985)

9 T.W. Ebbesen, Carbon Nanotubes Preparation and Properties, CRC Press (1997)

10 M. Endo, *CHEMTECH*, 18, 568 (1988)

11 Z. Liu, L.M. Gan, L. Hong, W. Chen, J.Y. Lee, *Journal of Power Sources*, 139, 73 (2005)

12 K.A. Klinedinst, W.M. Vogel, P. Stonehart, *J. Materials Science*, 11, 794 (1976)

13 W. Li, C. Liang, W. Zhou, H. Han, Z. Wei, G. Sun, Q. Xin, *Carbon*, 40, 787 (2002)

14 C. Journet, W.K. Maser, P. Bernier, A. Loiseau, M. Lamy de la Chapelle, S. Lefrant, P. Deniard, R. Leek, J.E. Fischer, *Nature*, 388, 756 (1997)

15 http://web.mit.edu/nanoengineering/research/nanotubes.shtml

16 M.S. Dresselhaus, G. Dresselhaus, P.C. Eklund, *Science of Fullerenes and Carbon Nanotubes*, Academic Press, San Diego (1996)

17 R.D. Johnson, G. Meijer, D.S. Bethune, *J. Am. Chem. Soc.*, 112, 8983 (1990)

18 K. Tanaka, T. Yamabe, K. Fukui, *The Science and Technology of Carbon Nanotubes*, Elsevier (1999)

19 S. Iijima, *Nature,* 354, 56 (1991)

20 J.E. Fischer, H. Dai, A. Thess, R. Lee, N.M. Hanjani, D.L. Dehaas, R. E. Smalley, *Physical Rev.B*, 55, 8, 4921 (1997)

21 T.W. Odom, J.L. Huang, P. Kim, C.M. Lieber., *Nature*, 391, 62 (1998)

22 S. Ijima, T. Ichihashi, *Nature*, 363, 603 (1993)

23 D.S. Bethune, C.H. Kiang, M.S. de Vries, G. Gorman, R. Savoy, J. Vazquez, R. Beyers, *Nature*, 363, 605 (1993)

24 M. Endo, H.W. Kroto, *J. Phys. Chem.,* 96, 6941 (1992)

25 S. Iijima, T. Ichihashi, Y. Ando, *Nature*, 356, 776 (1992)

26 R. Saito, M. Fujita, G. Dresselhaus, M.S. Dresselhaus, *Appl. Phys. Lett.,* 60, 2204 (1992)

27 J.W.G. Wildöer, L.C. Venema, A.G. Rinzler, R.E. Smalley, C. Dekker, *Nature,* 391, 59 (1998)

28 P.J. Harris, *Carbon Nanotubes And Related Structures*, Cambridge University Press (1999)

29 H. Kuzmany, J. Fink, M. Mehring, S. Roth, *Electronic Properties of Molecular Nanostructures*, American Institute of Physics (2003)

30 M.S. Strano, S.K. Doorn, E.H. Haroz, C. Kittrell, R.H. Hauge, R.E. Smalley, Nano Lett., Vol.3, 8, 1091 (2003)

31 A. Thess, R. Lee, P. Nikolaev, H. Dai, P. Petit, J. Robert, C. Xu, Y.H. Lee, S.G. Kim, A.G. Rinzler, D.T. Colbert, G.E. Scuseria, D. Tománek, J.E. Fischer, R.E. Smalley, *Science,* 273, 483 (1996)

32 Mc Elrath et al., *Patent Application Publication*, US 2004/0197638 A1 (2004)

33 M. Shiraishi, M. Ata, *Synthetic Metals*, 128, 235 (2002)

34 S.R. Broadbent, J.M. Hammersley, *Cam. Phil. Soc.*, 53, 629 (1957)

35 T. Takenobu, T. Takahashi, T. Kanbara, K. Tsukagoshi, Y. Aoyagi, Y. Iwasa, *Appl. Phys. Lett.*, 88, 033511 (2006)

36 M. Kaempgen, G.S. Duesberg, S. Roth, *Appl. Surf. Sci.*, 252 (2), 425, (2005)

37 Fleckner et al., United States Patent, *US 6,589,682 B1* (2003)

38 M. Kaempgen, M. Lebert, M. Haluška, N. Nicoloso, S. Roth, *Adv. Mat.*, 20, 616 (2008)

39 M. Kaempgen, M. Lebert, N. Nicoloso, S. Roth, *Appl. Phys. Lett.*, 92, 094103 (2008)

40 S. Roth, M. Lebert, M. Kaempgen, N. Nicoloso, *German patent application* 10 2007 012 235.9-45 (2007)

41 M. Chhowalla, K.B.K. Teo, C. Ducati, N.L. Rupesinghe, G.A.J. Amaratunga, A.C. Ferrari, D. Roy, J. Robertson, W.I. Milne, *J. Appl. Phys.*, 90, 10, 5308 (2001)

42 D. Tománek, R.J. Enbody, *Science and Application of Nanotubes*, Kluwer Academic/Plenum Publishers (2000)

43 M. Wienecke, M.-C. Bunescu, M. Pietrzak, K. Deistung, P. Fedtke, *Synthetic Metals*, 138, 165 (2003)

44 E. Frackowiak, G. Lota, T. Cacciaguerra, F. Béguin, *Electrochem. Comm.*, 8, 129 (2005)
45 Y. Tu, Y. Lin, Z.F. Ren, *Nano Letters,* 3, 1, 107 (2003)
46 X. Wang, W. Li, Z. Chen, M. Waje, Y.Yan, *Journal of Power Sources,* 158, 154 (2006)
47 H.C. Choi, M. Shim, S. Bangsaruntip, H. Dai, *J. Am. Chem. Soc*., 124, 31, 9059 (2002)
48 J.L. Bahr, J.M. Tour, *J. Mater. Chem.*, 12, 1952 (2002)
49 J.Z. Luo, L.Z. Gao, Y.L. Leung, C.T. Au, *Catal. Lett.*, 66, 91 (2000)
50 Y. Otake, B.G. Jenkins, *Carbon*, 31, 109 (1993)
51 G. de la Torre, W. Blau and T. Torres, *Nanotechnology*, 14, 765 (2003)
52 W. Du, L. Wilson, J. Ripmeester, R. Dutrisac, B. Simard, S. Denommee, NanoLetters, 2, 343 (2002)
53 P.M. Ajayan, T.W. Ebbesen, T. Ichihashi, S. Iijima, K. Tanigaki, H. Hiura, *Nature*, 362, 552 (1993)
54 M. Quintus, *Diss.*, Stuttgart (2002)
55 E. Papirer, J. Dentzer, S. Li, J.B. Donnet, *Carbon*, 29, 69 (1991)
56 H. Hiura, T.W. Ebbesen, K. Tanigaki, *Adv. Mater.*, 7, 275 (1995)
57 D.B. Mawhinney,.V. Naumenko, A. Kuznetsova, J.T. Yates Jr., J. Liu, R.E. Smalley, *Chem. Phys. Lett.*, 324, 213 (2000)
58 A. Kuzntesova, I. Popova, J.T. Yates Jr., M.J Bronikowski, C.B. Huffman, J. Liu, R.E. Smalley, H.H. Hwu, J.G. Chen, *J. Am. Chem. Soc.*, 123, 10699 (2001)
59 S. Pekker, J.-P. Salvetat, E. Jakab, J.-M. Bonard, L. Forró, *J. Phys. Chem.* B, 1999, 105, 7938 (2001)
60 N. Krishnankutty, M.A. Vannice, *Chem. Mater.* 7, 754 (1995)
61 V. Krstic; G.S. Duesberg, J. Muster, , M. Burghard, S. Roth, *Chem. Mater.*, 10, 2338 (1998)
62 F. Rohmund, L.K. Falk, E. Campbell, *Iron Catalyzed Growth of Carbon Nanotubes*, XIV International Winterschool/Euroconference, Kirchberg, 4-11 March, American Physics Institute (2000)
63 R.S. Lee, H.J. Kim, J. Fischer, A. Thess, R.E. Smalley, *Nature*, 388, 255 (1997)
64 S. Kazaoui, N. Minami, R. Jacquemin, H. Kataura, Y. Achiba, *Phys. Rev. B*, 60, 13339 (1999)

65 A.M. Rao, E. Richter, S. Bandow, B. Chase, P.C. Eklund, K.A. Williams, S. Fang, K.R. Subbaswamy, M. Menon, A. Thess, R.E. Smalley,G. Dresselhaus, M.S. Dresselhaus, Science, 275, 187 (1997)

66 S. G. Dresselhaus, P.C. Eklund, *Intercalation compounds of graphite*, Advances in Physics 51, 1 (2002)

67 M.P. Conrad, H.L. Strauss, *Phys. Rev. B*, 31, 6669 (1985)

68 O. Zhou et al., *Science*, 263, 1744 (1994)

69 S. Suzuki, M. Tomita, *J. Appl. Phys.,* 79, 3739 (1996)

70 C. Bower, A. Kleinhammes, Y. Wu, O. Zhou, *Chem. Phys. Lett.*, 288, 481 (1998)

71 W.C. Forsman, F.L. Vogel, D.E. Carl, J. Hoffman, *Carbon*, 16, 269 (1978)

72 F. Hennrich, R. Wellmann, S. Malik, S. Lebedkin, M.M. Kappes, *Phys. Chem. Chem. Phys.*, 5, 178 (2003)

73 J.O'M. Bockris, S.U.M. Khan, *Surface Electrochemistry – A Molecular Level Approach*, Plenum Press, New York (1993)

74 C.H. Hamann, W. Vielstich, A. Hamnett, Electrochemistry, Wiley-VCH, Weinheim (1998)

75 K. Ledjeff, *Brennstoffzellen*, C.F. Müller (1995)

76 U.S. Department of Energy, *Fuel Cell Handbook (Fifth Edition*), DE-AM26-99FT 40575 (2000)

77 Gottesfeld/Zawodzinski, Polymer Electrolyte Fuel Cells, Advances in Electrochemical Science and Engineering, Wiley-VCH (1998)

78 D. Linden, Handbook of Batteries and Fuel Cells, McGraw-Hill (1984)

79 N.N. Greenwood, A. Thompson, *J. Chem. Soc.*, 3485 (1959)

80 K.D. Kreuer, J.C. Lassègues, D. Rodriguez, *Solid State Ionics*, 61, 41 (1993)

81 J. Scholta, *Diss.*, Darmstadt (1993)

82 M. Carmo, V.A. Paganin, J.M. Rosolen, E.R. Gonsalez, *Journal of Power Sources*, 142, 169 (2005)

83 B.T. Tay, K.P. Ang, H. Gunasingham, *Analyst*, 113, 617 (1988)

84 E-TEK, Gas Diffusion Electrode: Catalyzed ELAT, technical product information (2003)

85 G. Stäb, *Diss.*, Ulm (1999)

86 O. Antoine, R. Durand, *Electrochemical and Solid-State Letters*, 4 (5) A55 (2001)

87 E.A. Ticianelli, C.R. Derouin, S. Srinivasan, *J. Electroanal. Chem*., 251, 275 (1988)

88 A.B. Hart, G.J. Womack, *Fuel Cells*, Chapman and Hall (1967)

89 T.J. Schmidt, M. Noeske, H.A. Gasteiger, R.J. Behm, P. Britz, W. Brijoux, H. Bönnemann, *Langmuir*, 13, 2591 (1997)

90 S. Srinivasan, *J. Electroanal. Chem.*, 118, 51 (1981)

91 M. Peuckert, T. Yoneda, R.A. Dalla Betta, M. Boudart, *J. Electrochem. Soc.* 133, 944 (1986)

92 R. Mosdale, P. Stevens, *Solid State Ionics* 61, 251 (1993)

93 K.F. Blurton, P. Greenberg, H.G. Oswin, D.R. Rutt, *J. Electrochem. Soc.*, 119, 5, 559 (1972)

94 A. Gamez, D. Richard, P. Gallezot, F. Gloaguen, R. Faure, R. Durand *Electrochimica Acta,* 41, 2, 307 (1996)

95 C. Wang, M. Waje, X. Wang, J.M. Tang, R.C. Haddon, Y. Yan, *Nano Lett.*, 4, 345 (2004)

96 E.J. Taylor, E.B. Anderson, N.R.K. Vilambi, *J. Electrochem. Soc.,* 139, 5 (1992)

97 M.Watanabe, M. Tomikawa, S. Motoo, *J. Electroanal. Chem.,* 182, 193 (1985)

98 S. Mukerjee, S. Srinivasan, J. Appleby, *Electrochimica Acta*, 38, 12, 1661 (1993)

99 S.Y. Cha, W.M. Lee, *J. Electrochem. Soc.*, 146, 4055 (1999)

100 R.O'Hayre, S.J. Lee, S.W. Cha, F.B. Prinz, *Journal of Power Sources,* 109, 483 (2002)

101 N. Cunningham, E. Irissou, M. Lefèvre, M.-C. Denis, D. Guay, J.-P. Dodelet, *Electrochemical and Solid-State Letters*, 6 (7) A125 (2003)

102 K. Kordesch, S. Jahangir, M. Schautz, *Electrochimica Acta*, 29, 11, 1589 (1984)

103 P. Colomban, Proton conductors- Solids, membanes and gels- materials and devices, Cambridge University Press (1992)

104 M. Hogarth, X. Glipa, *High Temperature Membranes For Solid Polymer Fuel Cells*, ETSU F/02/00189/REP, Johnson Matthey Technology Centre (2001)

105 *Unidym®*, CA, USA (www.unidym.com, former *Carbon Nanotechnlogies, CNI®*)

106 *Sigma-Aldrich®* (www.sigmaaldrich.com)

107 *GE Osmonics Labstore®* (www.osmolabstore.com)

108 F.W. Hyde, M. Alberg, K. Smith, *J. Ind. Microbiol. & Biotech*, 19, 142 (1997)

109 K.A. Klinedinst, W.M. Vogel, P. Stonehart, *Journal of Materials Science*, 12, 693 (1977)

110 A.J. Bard, L.R. Faulkner, *Electrochemical Methods- Fundamentals and Applications*, 2nd ed., John Wiley& Sons (2001)

111 M. Ashino, D. Obergfell, M. Haluška, S. Yang, A.N. Khlobystov, S. Roth, R. Wiesendanger, *Nature Nanotechnology*, 3, 337 (2008)

112 M. Haluška, M. Hulman, B. Hornbostel, J. Čech, V. Skákalová, S. Roth, *Physica Status Solid b*, 243, 13, 3042 (2006)

113 T. Takenobu, T. Takahashi, T. Kanbara, K. Tsukagoshi, Y. Aoyagi, Y. Iwasa, *Appl. Phys. Lett.*, 88, 033511 (2006)

114 J. Schindler, J. Brilla, N. Fruehauf, J. P. Novak, Z. Yaniv, *Phys. E*, 37, 119 (2007)

115 E. Artukovic, M. Kaempgen, D.S. Hecht, S. Roth, G. Gruner, *Nano Lett.*, 5, 757 (2005)

116 C. Niu, E.K. Sichel, R. Hoch, D. Moy, H. Tennent, *Appl. Phys. Lett.*, 70, 1480 (1997)

117 J.N. Barisci, G.G. Wallace, R.H. Baughman, *J. Electroanal. Chem.*, 488, 92 (2000)

118 S. Claye, J.E. Fischer, C.B. Huffman, A.G. Rinzler, R.E. Smalley, J. *Electrochem. Soc.*, 147, 2845 (2000)

119 S.H. Ng, J. Wang, Z.P. Guo, J. Chen, G.X. Wang, H.K. Liu, *Electrochim. Acta*, 51, 23 (2005)

120 M.E. Itkis, S. Niyogi, M.E. Meng, M.A. Hamon, H. Hu, and R.C. Haddon, *Nanoletters*, 2, 2, 155 (2002)

121 D.S. Hecht, L. Hu, G. Gruner, *Appl. Phys. Lett.*, 89, 13311 (2006)

122 M. Kaempgen, G.S. Duesberg, S. Roth, *Appl. Surf. Sci.*, 252 (2), 425, (2005)

123 D.J. Bae et al., Transport phenomena in an anistropically aligned single-wall carbon nanotube film, *Physical Review B*, 64, 233401 (2001

124 A.D. Bozhko, D.E. Sklovsky, V.A. Nalimova, A.G. Rinzler, R.E. Smalley, J.E. Fischer, *Appl. Phys. A,* 67, 75 (1998)

125 Y. Xing, L. Li, C.C. Chusuei, R.V. Hull, *Langmuir*, 21, 4185 (2005)

126 K.F. Blurton, H.R. Kunz, D.R. Rutt, *Electrochim. Acta*, 23, 183 (1978)

127 T.D. Gierke, G.E. Munn, F.C. Wilson, *J. Polym. Sci. Polym. Phys.*, 19, 1687 (1981)

128 M.S. Strano, *J. Am. Chem. Soc.*, 125, 16148 (2003)

129 M. Cinke, J. Li, B. Chen, A. Cassell, L. Delzeit, J. Han, M. Meyyappan, *Chem. Phys. Lett.*, 365, 69 (2002)

130 Z. Dehouche, L. Lafi, N. Grimard, J. Goyette, R Chahine, *Nanotechnology*, 16, 402 (2005)

131 M. Haluška, *internal communication*, Max-Planck-Institue for Solid State Research, Stuttgart (2006)

132 T.V. Sreekumar, T.Liu, S. Kumar, L.M. Ericson, R.H. Hauge, R.E. Smalley, *Chem. Mater.*, 15, 175 (2003)

133 V. Skákalová, A.B. Kaiser, U. Dettlaff-Weglikowska, K. Hrnčariková, S. Roth, *J. Phys. Chem.* B, 109, 7174 (2005)

134 S.K. Doorn, M.S. Strano, M.J. O'Connell, E.H. Haroz, K.L. Rialon, R.H. Hauge, and R.E. Smalley, *J. Phys. Chem*. B, 107, 6063 (2003)

135 C.G. Salzmann, S.A. Llewellyn, G. Tobias, M.A.H. Ward, Y. Huh, M.L.H. Green, *Adv. Mat.,* 19, 883 (2007)

136 M. Haluška, D. Obergfell, J.C. Meyer, G. Scalia, G. Ulbricht, B. Krauss, D.H. Chae, T. Lohmann, M. Lebert, M. Kaempgen, J. Smet, M. Hulman, S. Roth, K. von Klitzing, *physica status solidi (b)*, 244, 11, 4143 (2007)

137 J.S. Bradley, *Clusters and Colloids* (Ed.: G. Schmid), 459, VCH Weinheim (1994)

138 Q. Cao, S.H. Hur, Z.T. Zhu, Y. Sun, C. Wang, M. A. Meitl, M. Shim, J. A. Rogers, *Adv. Mater.*, 18, 304 (2006)

139 K.L. Lu, R.M. Lago, Y.K. Chen, M.L.H. Green, P. J. F. Harris, S. C. Tsang, *Carbon*, 34, 814 (1996)

140 H. Murphy, P. Papakonstantinou, T.I.T. Okpalugo, *J. Vac. Sci. Technol. B,* 24, 715 (2006)

141 P.G. Collins, K. Bradley, M. Ishigami, A. Zettl, *Science*, 287, 1801, (2000)

142 S.H. Jhi, S.G. Louie, M.L. Cohen, *Phys. Rev. Lett.*, 85, 1710 (2000)

143 C.M. Yang, K. Kaneko, M. Yudasaka., S. Iijima, *Nanoletters*, 2, 4, 385 (2002)

144 N. Nicoloso, M. Söhn, S. Roth, U. Dettlaff, M. Lebert, *WP 7: Fuel Cells, Canape Meeting*, Bologna, June 22 (2005)

145 Y.F. Yin, T. Mays, B. McEnaney, *Langmuir*, 15, 8714 (1999)

146 B.J. Hinds, N. Chopra, T. Rantell, R. Andrews, V. Gavalas, L.G. Bachas, *Science*, 303, 62 (2004)

147 Schröter et al., *Chemie*, VEB Fachbuchverlag Leibzig (1986)

148 *DuPont®* (www2.dupont.com)

149 J. Bett, J. Lundquist, *Electrochimica Acta*, 173, 18, 343 (1972)

150 Q. Li, J.O. Jensen, C. Pan, V. Bandur, M.S. Nilsson, F. Schönberger, A. Chromik, M. Hein, T. Häring, J. Kerres, N.J. Bjerrum, *Fuel Cells*, 3–4, 188 (2008)

151 C. Henschel, *Fuel Cells Bull.*, 2, 12 (2006)

152 K.H. Yoon, J.Y. Choi, J.H. Jang, Y.S. Cho, K.H. Jo, *J. Appl. Electrochem.*, 30, 121 (2000)

153 L. Delzeit, I.M. Aninch, B.A. Cruden, D. Hash, B. Chen, J. Han, M. Meyyappan, *J. Appl. Phys.*, 91, 9, 6028 (2002)

154 M. Lebert, M. Kaempgen, M. Soehn, T. Wirth, S. Roth, N. Nicoloso, *Catalysis Today*, in press, online 23 December (2008)
155 G. Che, B.B. Lakshmi, C.R. Martin, *Nature*, 393, 346 (1998)
156 J. Yang, D.J. Liu, *Carbon*, 45, 14, 2845 (2007)
157 T. Hatanaka, H. Nakanishi, S.I. Matsumoto, Y. Morimoto, 210th ECS Meeting Cancun (Mexico): *The Electrochemical Society*, 549 (2006)
158 D. Ugarte, A. Châtelain, W.A. de Heer, *Science*, 274, 1897 (1996)
159 http://hyperphysics.phy-astr.gsu.edu/hbase/surten.html
160 C. Dellago, M. Naor, G. Hummer, *Physical Review Letters*, 90, 10 (2003)
161 V.P. Sokhan, D. Nicholson, *J. Chem. Phys.*, 117, 8531 (2002)
162 S. Supple, Quirke, *Phys. Rev. Lett.*, 90, 214501 (2003)
163 J.J. Jasper, *J. Phys. Chem*., Ref. Data, I(4), 841 (1972)
164 O.A. Nerushev, M. Sveningsson, L.K.L. Falk, F. Rohmund, *J. Mater. Chem.*, 11, 1122 (2001)
165 H. Kanzow, C. Lenski, A. Ding, *Phys. Rev. B*, 6312, 5402 (2001)
166 http://www.parylene.com/technology/PTC-Parylene-Proporties-Chart-2007.pdf
167 X. Zhao,Y. Ando, L.-C. Qin, H. Kataura,Y. Maniwa, R. Saito, *Chem. Phys. Lett*., 361, 169 (2002)
168 R. Andrews, D. Jacques, A.M. Rao, F. Derbyshire, D. Qian, X. Fan, E.C. Dickey, J. Chen, *Chem. Phys. Lett.*, 303, 467 (1999)
169 K.K.S. Lau, J. Bico, K.B.K. Teo, M. Chhowalla, G.A.J. Amaratunga, W.I. Milne, G.H. McKinley, K.K. Gleason, *Nano Letters*, 3, 12, 1701 (2003)
170 H. Kuzmany, J. Fink, M. Mehring, S. Roth, *Electronic Properties of Molecular Nanostructures*, American Institute of Physics (2002)
171 C. Journet, S. Moulinet, C. Ybert, S. T. Purcell and L. Bocquet, *Europhys. Lett.*, 71, 1, 104 (2005)
172 H.-F. Cui, J.-S. Ye, W.-D. Zhang, J.Wang, F.-S. Sheu, *J. Electroanal. Chem.*, 577, 295 (2005)
173 G. Che, B.B. Lakshmi, C.R. Martin, E.R. Fisher, *Chem. Mater.*, 10, 260 (1998)
174 D. Qian, E.C. Dickey, R. Andrews, T. Rantell, *Appl. Physics Letters*, 76, 20, 2868 (2000)
175 R.R.A. Callahan, G.B. Raupp, S.P. Beaudoin, *J. Vac. Sci. Technol. B,* 19(3), 725 (2001)
176 R.D. Tacito, C. Steinbrüchel, *J. Electrochem. Soc.*, 143, 1974 (1996)

177 H. Cui, O. Zhou, B.R. Stoner, *J. Appl. Phys*., 88, 6072 (2000)

178 T. Standaert, P.J. Matsuo, X. Li, G.S. Oehrlein, T.M. Lu, R. Gutmann, C.T. Rosenmayer, J.W. Bartz, J.G. Langan, W.R. Entley, *J. Vac. Sci. Technol. A*, 19(2), Mar/Apr (2001)

179 Carbon Nanotechnlogies Inc. (CNI), *Invoice* (2003)